

See discussions, stats, and author profiles for this publication at: <https://www.researchgate.net/publication/274635279>

Fluid model of the sheath in front of a floating electrode immersed in a magnetized plasma with oblique magnetic field: Some comments on ion source terms and ion temperature effect...

ARTICLE *in* PHYSICS OF PLASMAS · APRIL 2015

Impact Factor: 2.14 · DOI: 10.1063/1.4916318

READS

68

1 AUTHOR:



[Tomaz Gyergyek](#)

University of Ljubljana

103 PUBLICATIONS 329 CITATIONS

[SEE PROFILE](#)

Fluid model of the sheath in front of a floating electrode immersed in a magnetized plasma with oblique magnetic field: Some comments on ion source terms and ion temperature effects

T. Gyergyek and J. Kovačič

Citation: *Physics of Plasmas* (1994-present) **22**, 043502 (2015); doi: 10.1063/1.4916318

View online: <http://dx.doi.org/10.1063/1.4916318>

View Table of Contents: <http://scitation.aip.org/content/aip/journal/pop/22/4?ver=pdfcov>

Published by the AIP Publishing

Articles you may be interested in

[A unified analysis of plasma-sheath transition in the Tonks–Langmuir model with warm ion source](#)
Phys. Plasmas **21**, 073503 (2014); 10.1063/1.4885638

[Multiple ion species plasmas with thermal ions in an oblique magnetic field](#)
Phys. Plasmas **20**, 083501 (2013); 10.1063/1.4817262

[Kinetic Lagrange simulation of a source-driven magnetized oblique presheath](#)
Phys. Plasmas **12**, 103506 (2005); 10.1063/1.2098367

[Ion kinetic effects in radio-frequency sheaths](#)
Phys. Plasmas **12**, 033505 (2005); 10.1063/1.1857915

[Plasma-surface interaction model with secondary electron emission effects](#)
Phys. Plasmas **11**, 1220 (2004); 10.1063/1.1647567



Fluid model of the sheath in front of a floating electrode immersed in a magnetized plasma with oblique magnetic field: Some comments on ion source terms and ion temperature effects

T. Gyergyek^{1,2} and J. Kovačič²

¹University of Ljubljana, Faculty of Electrical Engineering, Tržaška 25, 1000 Ljubljana, Slovenia

²Jožef Stefan Institute, Jamova 39, POB 100, 1000 Ljubljana, Slovenia

(Received 11 November 2014; accepted 13 March 2015; published online 6 April 2015)

A one-dimensional fluid model of the magnetized plasma-wall transition region in front of a floating electrode immersed in a magnetized plasma with oblique magnetic field is presented. The Boltzmann relation is assumed for the electrons, while the positive ions obey the ion continuity and momentum exchange equation. The ions are assumed to be isothermal. By comparison with a two-fluid model, it is shown that assuming the Boltzmann relation for the electrons implies that there is no creation or annihilation of the electrons. Consequently, there should not be any creation and annihilation of the positive ions either. The models that assume the Boltzmann relation for the electrons and a non-zero ion source term at the same time are therefore inconsistent, but such models have nevertheless been used extensively by many authors. So, in this work, an extensive comparison of the results obtained using the zero source term on one hand and three different non-zero source terms on the other hand is made. Four different ion source terms are considered in total: the zero source term and three different non-zero ion source terms. When the zero source term is used, the model becomes very sensitive to the boundary conditions, and in some cases, the solutions exhibit large amplitude oscillations. If any of the three non-zero ion source terms is used, those problems are eliminated, but also the consistency of the model is broken. The model equations are solved numerically in the entire magnetized plasma-wall transition region. For zero ion temperature, the model can be solved even if a very small ion velocity is selected as a boundary condition. For finite ion temperature, the system of equations becomes stiff, unless the ion velocity at the boundary is increased slightly above the ion thermal velocity. A simple method how to find a solution with a very small ion velocity at the boundary also for finite ion temperature in the entire magnetized plasma-wall transition region is proposed. © 2015 AIP Publishing LLC.

[<http://dx.doi.org/10.1063/1.4916318>]

I. INTRODUCTION

In recent years, many papers have been published describing the magnetized plasma-wall transition region in front of a negatively biased wall immersed in a plasma under the action of a constant magnetic field. Among these works is Chodura's model, which describes the pre-sheath of a collision-less plasma in an oblique magnetic field.¹ In his model, Chodura shows that there exists a magnetic pre-sheath; in this work, it is called the Chodura layer, where the ions enter with a velocity V_{par} parallel to the magnetic field equal to the sound speed V_s . After this layer, there is the sheath, a collision-less charged region that begins when the component of the positive ion velocity perpendicular to the wall V_{ix} reaches the sound speed V_s . In the Chodura layer, the electric field grows causing the velocity of the positive ions to deviate from the magnetic-field lines. The situation is illustrated schematically in Fig. 1. Several authors extend this model including collisions as a pre-sheath mechanism,^{2–7} ionization,⁸ or both ionization and collisions.⁹ Recently, a rather comprehensive kinetic analysis, where the boundaries of the Chodura layer have been precisely defined, has been published.¹⁰ In the last years, the use of the Boltzmann relation for the electrons when there is a

magnetic field present has been reexamined by several authors.^{11–13} Also, in recent years, many other specific aspects of the sheath in an oblique magnetic field have been analyzed. For example, effects of ion collisions have been analyzed;^{14–18} positive ion temperature effects have also

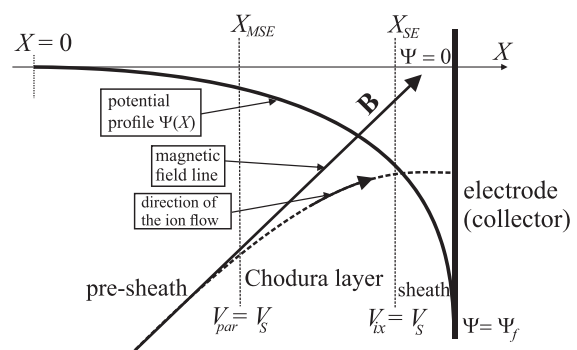


FIG. 1. Illustration of the pre-sheath, Chodura layer, and the sheath. Here, V_{ix} is the component of the velocity of the ion flow perpendicularly to the electrode (formula (23) below), V_s is the ion sound velocity (formula (26) below), the parallel ion velocity V_{par} is given by the formula (37) below, X_{MSE} is the position of the magnetized pre-sheath edge, X_{SE} is the position of the sheath edge, and Ψ_f is the floating potential of the collector - formula (47) below. The Chodura layer lies between X_{MSE} and X_{SE} .

attracted attention.^{19–24} Some authors analyzed the effects of the presence of two^{25–29} or even multiple³⁰ species of positive ions. The sheath in a magnetized plasma in the presence of negative ions has been studied,^{31–35} and even a combination of the presence of two positive and one negative ion species has been taken into account.^{36,37}

In the majority of the above mentioned papers, fluid models are used, although more sophisticated approaches like two fluid models^{38,39} or particle-in-cell computer simulations^{40–43} have also been used. Fluid models are based on the continuity equation and momentum exchange equation for ions—Eqs. (1) and (2) below—while the electrons are usually assumed to be Boltzmann distributed—Eq. (3) below—in spite of the second thoughts expressed by some authors^{11–13} about the validity of such an assumption in a magnetized plasma. The potential profile is determined by the Poisson equation—Eq. (4) below. In some recent papers, where the presence of a second positive ion species is taken into account, two continuity and two momentum exchange equations are written—one pair of equations for each positive ion species—see, e.g., Refs. 26 and 28. If negative ions are present in the plasma, these ions are very often also taken as Boltzmann distributed,^{31–35,37} but with lower temperature than electrons. The ion continuity Eq. (1) has a so called ion source term S_i on the right hand side. The same term appears also in the momentum exchange Eq. (2). This term is a function that describes creation of ions in the system. The form of this function is assumed. In the literature, two forms of S_i can be found. Very often, the so called zero ion source term (formula (12) below) is assumed. Such assumption has been made by many authors—see, e.g., Refs. 2, 16, 17, 19–21, 24–30, 34, 36, 45, and 46. Another rather common assumption is that the ionization is proportional to the local electron density. In this work, such source term is called the exponential source term (formula (14) below), since the Boltzmann distribution is assumed for the electron density. The exponential source term has also been used by many authors—see, e.g., Refs. 3, 8, 9, 18, 22, 23, 32, 33, 35, 37, 42, and 44. In this work, two additional simple forms of S_i are proposed, and the results obtained with the zero ion source term on one hand and with the non-zero ion source terms on the other are compared.

In Sec. II, the analytical model is presented. In Sec. III, some results of the model are shown. Attention is focused to the comparison of the results obtained using the zero ion source term on one hand and the non-zero ion source terms on the other hand. A simple method how to cope with a non-zero ion temperature is proposed and then applied to calculate the dependence of the floating potential, sheath potential drop, sheath thickness, thickness of the Chodura layer, and potential drop in the Chodura layer on ion temperature. In Sec. IV, a comparison with a two-fluid model is made, and it is shown that the assumption of the Boltzmann relation for the electron density is equivalent to the assumption that the electron source term in the electron continuity equation is zero. If only one positive ion species and electrons are present in the plasma, also the ion source term should be zero. The models, where the Boltzmann relation is assumed for the electrons and at the same time a non-zero ion source term is assumed for the positive ions, are therefore not self-consistent. In Sec. V, some conclusions are given.

II. MODEL

The model consists of continuity equation and momentum transport equation for ions

$$\frac{\partial n_i}{\partial t} + \nabla \cdot (n_i \mathbf{u}_i) = S_i, \quad (1)$$

$$m_i n_i \left(\frac{\partial \mathbf{u}_i}{\partial t} + (\mathbf{u}_i \cdot \nabla) \mathbf{u}_i \right) \\ = n_i e_0 (\mathbf{E} + \mathbf{u}_i \times \mathbf{B}) - \nabla p_i + \mathbf{A}_i - m_i \mathbf{u}_i S_i, \quad (2)$$

the Boltzmann relation for the electrons

$$n_e(\mathbf{r}) = n_0 \exp \left(\frac{e_0 \Phi(\mathbf{r})}{k T_e} \right), \quad (3)$$

and the Poisson equation

$$\nabla^2 \Phi(\mathbf{r}) = -\frac{e_0}{\varepsilon_0} (n_i(\mathbf{r}) - n_e(\mathbf{r})). \quad (4)$$

The meaning of the symbols is standard: e_0 is the elementary charge, m_i is the ion mass, n_i is the ion density, \mathbf{u}_i is the average ion velocity, which has the components $\mathbf{u}_i = (u_{ix}, u_{iy}, u_{iz})$, $\mathbf{r} = (x, y, z)$ is the space vector, Φ is the potential, \mathbf{E} is the electric field, \mathbf{B} is the magnetic field, p_i is the ion pressure, \mathbf{A}_i is the collisional momentum transfer term, and S_i is the ion source term. The symbol n_0 denotes the electron density at the location, where the potential Φ is zero—this means somewhere far away from any boundaries of the plasma system. Note that at this location also the ion density is n_0 and the plasma is neutral. The Boltzmann constant is k , and T_e is the electron temperature.

Eqs. (1) and (2) form a system of four differential equations with five unknown functions; so one additional equation is needed to close the system. The hierarchy chain of hydrodynamic equations derived from the kinetic equation must be cut at a certain level by some ad hoc assumption. A simple and widely used approach (used also in this work) is to use only the continuity equation and the momentum balance equation. In this case, gradient pressure force ∇p_i must be expressed by two lower moments of the velocity distribution function, which are the density n_i and the velocity of the ion flow \mathbf{u}_i . Very often ideal gas law is used for this purpose

$$p_i(\mathbf{r}) = k T_i(\mathbf{r}) n_i(\mathbf{r}). \quad (5)$$

Unfortunately, Eq. (5) does not close the system of equations, since an additional new unknown function $T_i(\mathbf{r})$ is introduced and one has to deal with five equations and six unknown functions. By taking into account (5), the gradient pressure force ∇p_i , which appears in (2), is written the following form:⁴⁷

$$\nabla p_i(\mathbf{r}) \equiv \nabla(k T_i(\mathbf{r}) n_i(\mathbf{r})) \equiv k T_i(\mathbf{r}) \nabla n_i(\mathbf{r}) + k n_i(\mathbf{r}) \nabla T_i(\mathbf{r}) \\ = \kappa(\mathbf{r}) k T_i(\mathbf{r}) \nabla n_i(\mathbf{r}). \quad (6)$$

In writing down the above equation, it has been assumed that the vectors ∇p_i , ∇T_i , and ∇n_i are parallel to each other. Kuhn *et al.*⁴⁷ call the above equation the local polytropic

law, and $\kappa(\mathbf{r})$ is called the local polytropic coefficient. If the model is reduced to be only one-dimensional model (see below), it can be seen more clearly that κ is indeed a space dependent quantity, rather than a constant. In one dimension, Eq. (6) becomes

$$\frac{dp_i}{dx} \equiv \frac{d}{dx}(kT_i n_i) \equiv kn_i \frac{dT_i}{dx} + kT_i \frac{dn_i}{dx} = \kappa kT_i \frac{dn_i}{dx}, \quad (7)$$

$$\kappa = 1 + \frac{n_i}{T_i} \frac{\frac{dT_i}{dx}}{\frac{dn_i}{dx}} = 1 + \frac{n_i}{T_i} \frac{dT_i}{dn_i}. \quad (8)$$

In Ref. 47, it was shown for a non-magnetized plasma that the polytropic function defined above has low values in the pre-sheath region, but then the value increases rapidly and reaches a maximum at the plasma-sheath boundary. In collision-less case, the maximum value of κ at the sheath edge can be rather high—up to almost 8. Inside the sheath, κ drops to the value around 3. This implies adiabatic ion flow in the sheath.

In order to close the system of equations formed by (1), (2), and (7), some assumption about the polytropic function (8) must be made. In order to keep the model as simple as possible, we assume that $\kappa = 1$, which implies constant ion temperature T_i . The gradient pressure force in one-dimensional model is then given by

$$\frac{dp_i}{dx} = kT_i \frac{dn_i}{dx}. \quad (9)$$

As recognized also in, e.g., Ref. 36, using the assumption (9) is an oversimplification, but, nevertheless, this approach is widely used in the literature when sheath in an oblique magnetic field and with non-zero ion temperature is studied.^{19–21,24,29,36}

The coordinate system is illustrated in Fig. 2. An infinitely large planar electrode—called collector—is perpendicular to the x axis. The magnetic field lies in the xy plane and has the components $\mathbf{B} = B(\sin \alpha, \cos \alpha, 0)$. As already mentioned above, our model is one-dimensional. We therefore assume that the electric field \mathbf{E} only has 1 component, which is related to the potential Φ by

$$E_x = -\frac{d\Phi}{dx}. \quad (10)$$

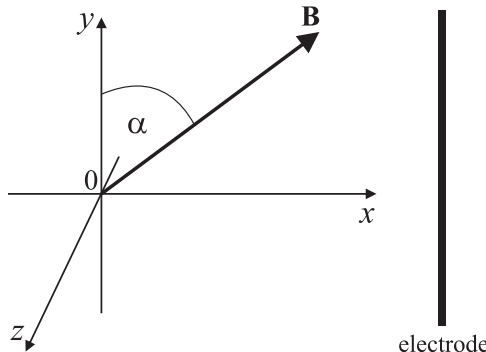


FIG. 2. The electrode (collector) lies in the yz plane, while the magnetic field lies in the xy plane. The components of the magnetic field are $\mathbf{B} = B(\sin \alpha, \cos \alpha, 0)$.

One-dimensional model implies that Φ , n_i , p_i , \mathbf{u}_i , S_i , and \mathbf{A}_i are functions of x only. The gradient and Laplace operators are replaced by derivatives over x

$$\nabla \rightarrow \vec{e}_x \frac{d}{dx}, \quad \nabla^2 \rightarrow \frac{d^2}{dx^2}. \quad (11)$$

The ion source term S_i gives the number of ions which are created or annihilated per unit volume and per unit time by some ionization mechanism. In the literature, various models are used. The first model assumes that the plasma contains only ions and electrons created by some plasma source, but beside that, there is no additional ionization anywhere in the system, although neutral atoms can also be present in such plasma system. In this case, the ion source term is zero,

$$S_i = 0, \quad (12)$$

and it is called the zero ion source term. Such source term has been used by several authors.^{2,16,17,19–21,24–30,34,36,45,46} The second model assumes a spatially uniform production of ion-electron pairs everywhere in the system with a constant rate τ

$$S_i = \frac{n_0}{\tau}. \quad (13)$$

The ion source term given by (13) is called the constant ion source term. Such situation could occur in a plasma that contains ions, electrons, and neutral atoms of the same species as ions. Assume that the system is irradiated uniformly by cosmic rays that ionize neutral atoms present in the plasma. The time τ is the average time between two consecutive ionizations. Since this source term has a simple form, it is surprising that we have not been able to find any example of the use of this term in the literature. The third ion source term is based on the assumption that neutral atoms, present in the plasma, are ionized when they collide with electrons. In this case, the ionization is proportional to the electron density. In our model, the electrons are assumed to be Boltzmann distributed (3), so in one-dimensional model, this source term is written as

$$S_i = \frac{n_e(x)}{\tau} = \frac{n_0}{\tau} \exp\left(\frac{e_0 \Phi(x)}{kT_e}\right). \quad (14)$$

This ion source term is called the exponential ion source term. Such ion source term has also been used by many authors who studied sheath in a magnetized plasma.^{3,8,9,18,22,23,32,33,35,37,42,44} The last ion source term considered in this work is written in the following form:

$$S_i = \frac{n_0}{\tau} \cos\left(\frac{\pi u_{ix}(x)}{2 c_s}\right) H(c_S - u_{ix}(x)). \quad (15)$$

Because the model is one-dimensional, u_{ix} depends only on x . The ion sound velocity c_s is defined below (formula (25)) and $H(x)$ is the Heaviside unit step function. This source term is called the cosine source term, and it is probably the most artificially constructed of all four source terms. It

assumes a situation where ionization rate decreases with increasing average ion velocity. When the ion sound velocity is reached at the sheath edge, the ionization drops to zero and then remains zero in the sheath. Mathematically, this is achieved with the Heaviside function.

The collisional momentum transfer term is labeled \mathbf{A}_i . The ions can lose momentum in elastic collisions with some other particle species. In our model, these particles can be electrons and neutral atoms. The rate of change of momentum of the ions because of such collisions is given⁴⁸ in the following way:

$$\mathbf{A}_i = -m_i n_i \sum_{\beta} \nu_{i\beta} (\mathbf{u}_i - \mathbf{u}_{\beta}).$$

Here, $\nu_{i\beta}$ is the frequency of the ion collisions with the particle species β , and \mathbf{u}_{β} is average velocity of these particles. In our case, the sum over β should go over neutral atoms and electrons. Note that elastic collisions of ions with neutrals are usually charge exchange collisions, while the collisions with electrons are coulomb collisions. It is beyond the scope of our work to analyze in detail the collisions of ions with various particle species. Also no attempt is made to estimate relative velocities of ions with respect to neutrals and electrons. Instead, the collisional momentum transfer term is simply taken in the following form:

$$\mathbf{A}_i = -m_i n_0 \nu \mathbf{u}_i. \quad (16)$$

Here, ν is simply some effective collision frequency of ions that includes collisions with neutrals and electrons. In addition, the collision term is taken to be simply proportional to the ion velocity \mathbf{u}_i , and no attempt is made to estimate relative ion velocity with respect to neutrals, electrons, or any other particle species.

The steady state is analyzed so the time derivatives are zero. Using the coordinate system shown in Fig. 2 and the assumptions described above, Eqs. (1) and (2) together with the Poisson Eq. (4) and gradient pressure force (9) are written in the following form:

$$\frac{dn_i}{dx} u_{ix} + n_i \frac{du_{ix}}{dx} = \left\{ \begin{array}{l} 0 \\ \frac{n_0}{\tau} \\ \frac{n_0}{\tau} \exp\left(\frac{e_0 \Phi(x)}{kT_e}\right) \\ \frac{n_0}{\tau} \cos\left(\frac{\pi u_{ix}(x)}{2 c_S}\right) H(c_S - u_{ix}(x)) \end{array} \right\}, \quad (17)$$

$$n_i m_i u_{ix} \frac{du_{ix}}{dx} + e_0 n_i \frac{d\Phi}{dx} + e_0 B \cos(\alpha) n_i u_{iz} + kT_i \frac{dn_i}{dx} + m_i n_0 u_{ix} \cdot \left\{ \begin{array}{l} \nu \\ \frac{1}{\tau} + \nu \\ \frac{1}{\tau} \exp\left(\frac{e_0 \Phi(x)}{kT_e}\right) + \nu \\ \frac{1}{\tau} \cos\left(\frac{\pi u_{ix}(x)}{2 c_S}\right) H(c_S - u_{ix}(x)) + \nu \end{array} \right\} = 0, \quad (18)$$

$$n_i m_i u_{ix} \frac{du_{iy}}{dx} - e_0 B \sin(\alpha) n_i u_{iz} + m_i n_0 u_{iy} \cdot \left\{ \begin{array}{l} \nu \\ \frac{1}{\tau} + \nu \\ \frac{1}{\tau} \exp\left(\frac{e_0 \Phi(x)}{kT_e}\right) + \nu \\ \frac{1}{\tau} \cos\left(\frac{\pi u_{ix}(x)}{2 c_S}\right) H(c_S - u_{ix}(x)) + \nu \end{array} \right\} = 0, \quad (19)$$

$$n_i m_i u_{ix} \frac{du_{iz}}{dx} - e_0 B \cos(\alpha) n_i u_{ix} + e_0 B \sin(\alpha) n_i u_{iy} + m_i n_0 u_{iz} \cdot \left\{ \begin{array}{l} \nu \\ \frac{1}{\tau} + \nu \\ \frac{1}{\tau} \exp\left(\frac{e_0 \Phi(x)}{kT_e}\right) + \nu \\ \frac{1}{\tau} \cos\left(\frac{\pi u_{ix}(x)}{2 c_S}\right) H(c_S - u_{ix}(x)) + \nu \end{array} \right\} = 0, \quad (20)$$

$$\frac{d^2 \Phi}{dx^2} = -\frac{e_0}{\varepsilon_0} \left(n_i - n_0 \exp\left(\frac{e_0 \Phi(x)}{kT_e}\right) \right). \quad (21)$$

The system (17)–(21) is a system of 5 differential equations for 5 unknown functions, which are three velocity components $u_{ix}(x)$, $u_{iy}(x)$, $u_{iz}(x)$, potential $\Phi(x)$, and density $n_i(x)$. In fact, the system (17)–(21) forms four systems of equations. Each of the systems corresponds to one of the four different ion source terms (12), (13), (14), or (15). The zero source term (12) corresponds to the top expression in braces, the constant source term (13) corresponds to the second term in the braces, the third expression in the braces corresponds to the exponential source term (14), and the bottom expression in the braces corresponds to the cosine source term (15). This system can be solved numerically, but before any solution is attempted, the system must be transformed into dimensionless form. For this purpose, the following variables are introduced:

$$\lambda_D = \sqrt{\frac{\varepsilon_0 kT_e}{n_0 e_0^2}}, \quad c_0 = \sqrt{\frac{kT_e}{m_i}}, \quad \omega_c = \frac{e_0 B}{m_i}, \quad K = \omega_c \tau, \quad L = c_0 \tau, \quad L_c = \frac{c_0}{\nu}, \quad (22)$$

$$r_{Li} = \frac{c_0}{\omega_c}, \quad N_i = \frac{n_i}{n_0}, \quad \Psi = \frac{e_0 \Phi}{kT_e}, \quad V_{ix} = \frac{u_{ix}}{c_0}, \quad V_{iy} = \frac{u_{iy}}{c_0}, \quad V_{iz} = \frac{u_{iz}}{c_0}, \quad \Theta = \frac{T_i}{T_e}, \quad \varepsilon = \frac{\lambda_D}{L}, \quad (23)$$

$$\mu = \frac{m_e}{m_i}, \quad Z = \nu \tau, \quad X = \frac{x}{L}, \quad \text{or} \quad X = \frac{x}{L_c}, \quad \text{or} \quad X = \frac{x}{\lambda_D}, \quad \text{or} \quad X = \frac{x}{r_{Li}}. \quad (24)$$

Here, λ_D is the well known Debye length, c_0 is the normalizing velocity, and L is the distance that an ion moving with the normalizing velocity passes in one ionization time τ . It is called ionization length. On the other hand, L_c is called the

TABLE I. The coefficients A_1 , A_2 , and A_3 that correspond to four different scalings of the space coordinate in the systems of Eqs. (27)–(31) and (33)–(36).

Coefficient	Scaling $X = \frac{x}{L}$	Scaling $X = \frac{x}{L_c}$	Scaling $X = \frac{x}{r_{Li}}$	Scaling $X = \frac{x}{\lambda_D}$
A_1	1	$\frac{1}{Z}$	$\frac{1}{K}$	ε
A_2	K	$\frac{K}{Z}$	1	εK
A_3	ε^2	$Z^2 \varepsilon^2$	$K^2 \varepsilon^2$	1

collision length or mean free path. This is the distance that an ion moving with the normalizing velocity passes between two collisions. The cyclotron frequency is ω_c , and r_{Li} is the Larmor radius of an ion that enters into the given magnetic field B with the normalizing velocity c_0 perpendicular to the magnetic-field lines. The potential Ψ is normalized to the electron temperature, the velocity components are normalized to the normalizing velocity c_0 , and the density is normalized to n_0 .

Note that the normalizing velocity c_0 is not the same as the ion sound velocity c_s , which is defined as (see, e.g., Refs. 49 and 50)

$$c_s = \sqrt{\frac{kT_e^* + \kappa kT_i}{m_i}}, \quad (25)$$

where T_e^* is the so called screening temperature.⁴⁹ It is defined as

$$T_e^* = \frac{e_0 n_-}{k \frac{dn_-}{d\Psi}}.$$

Here, n_- is the density of all the negatively charged particle species. In our case, we have only one Maxwellian electron population, so the screening temperature is equal to the electron temperature, $T_e^* = T_e$. Using the variables (22)–(24) and taking into account that $\kappa = 1$, the ion sound velocity (25) is written in the following way

$$V_S = \frac{c_s}{c_0} = \sqrt{1 + \Theta}. \quad (26)$$

There are obviously 4 length scales that appear in the problem: the Debye length λ_D , the ionization length L , the collision length L_c , and the Larmor radius r_{Li} . So, the space coordinate x can be normalized to any of them. In normalized variables, the system of Eqs. (17)–(21) is written in the following form:

$$\frac{dN_i}{dX} V_{ix} + N_i \frac{dV_{ix}}{dX} = \frac{d}{dX} (N_i V_{ix}) = A_1 S_1, \quad (27)$$

TABLE II. The coefficients S_1 and S_2 that correspond to four different source terms (12), (13), (14), or (15) in the systems of Eqs. (27)–(31) and (33)–(36).

Coefficient	Zero source term (12)	Constant source term (13)	Exponential source term (14)	Cosine source term (15)
S_1	0	1	$\exp(\Psi)$	$\cos\left(\frac{\pi V_{ix}}{2 V_S}\right) H(V_S - V_{ix})$
S_2	Z	$1 + Z$	$\exp(\Psi) + Z$	$\cos\left(\frac{\pi V_{ix}}{2 V_S}\right) H(V_S - V_{ix}) + Z$

$$N_i V_{ix} \frac{dV_{ix}}{dX} + N_i \frac{d\Psi}{dX} + \Theta \frac{dN_i}{dX} + A_2 \cos(\alpha) N_i V_{iz} + A_1 V_{ix} S_2 = 0, \quad (28)$$

$$N_i V_{ix} \frac{dV_{iy}}{dX} - A_2 \sin(\alpha) N_i V_{iz} + A_1 V_{iy} S_2 = 0, \quad (29)$$

$$N_i V_{ix} \frac{dV_{iz}}{dX} - A_2 \cos(\alpha) N_i V_{ix} + A_2 \sin(\alpha) N_i V_{iy} + A_1 V_{iz} S_2 = 0, \quad (30)$$

$$A_3 \frac{d^2 \Psi}{dX^2} = \exp(\Psi) - N_i. \quad (31)$$

The coefficients A_1 , A_2 , and A_3 must be taken from the respective column of Table I, according to the coordinate scaling that is selected. The coefficients S_1 and S_2 must be selected from the respective column of Table II, according to the ion source term (12), (13), (14), or (15) that is selected. So, Eqs. (27)–(31) represent, in fact, sixteen (4 ion source terms \times 4 scalings) systems of five differential equations for five unknown functions: $\Psi(X)$, $N_i(X)$, $V_{ix}(X)$, $V_{iy}(X)$, and $V_{iz}(X)$.

With the system (27)–(31), the problem can be studied in the entire magnetized plasma-wall transition region. But sometimes, the attention is limited only to the pre-sheath region, where the plasma quasi-neutrality is assumed a-priori. In this case, Poisson Eq. (31) is replaced by the neutrality condition

$$N_i(X) = \exp(\Psi(X)). \quad (32)$$

When (32) is inserted into (27)–(31), the system (27)–(31) is transformed into

$$\frac{d\Psi}{dX} = \frac{1}{V_{ix}} \left(A_1 \exp(-\Psi) S_1 - \frac{dV_{ix}}{dX} \right). \quad (33)$$

$$V_{ix} \frac{dV_{ix}}{dX} + \frac{d\Psi}{dX} (1 + \Theta) + A_2 \cos \alpha V_{iz} + A_1 V_{ix} \exp(-\Psi) S_2 = 0. \quad (34)$$

$$V_{ix} \frac{dV_{iy}}{dX} - A_2 \sin \alpha V_{iz} + A_1 V_{iy} \exp(-\Psi) S_2 = 0. \quad (35)$$

$$V_{ix} \frac{dV_{iz}}{dX} - A_2 \cos \alpha V_{ix} + A_2 \sin \alpha V_{iy} + A_1 V_{iz} \exp(-\Psi) S_2 = 0. \quad (36)$$

The system (33)–(36) forms sixteen systems of four differential equations for four unknown functions of X , which are: $\Psi(X)$, $V_{ix}(X)$, $V_{iy}(X)$, and $V_{iz}(X)$.

When the system (27)–(31) or the system (33)–(36) is solved, three velocity components are obtained, which together form a velocity vector $\mathbf{V}_i = (V_{ix}, V_{iy}, V_{iz})$. In the coordinate system shown in Fig. 2, the magnetic field has the components

$\mathbf{B} = (B \sin(\alpha), B \cos(\alpha), 0)$. It is convenient to separate the ion velocity vector \mathbf{V}_i into the part V_{par} , which is parallel to the magnetic field, and the part V_{perp} , which is perpendicular to the magnetic field. These two parts are given by

$$V_{par} = \frac{\mathbf{V}_i \cdot \mathbf{B}}{B} = V_{ix} \sin(\alpha) + V_{iy} \cos(\alpha), \quad (37)$$

$$V_{perp} = \frac{|\mathbf{V}_i \times \mathbf{B}|}{B} = \sqrt{V_{iz}^2 + (V_{ix} \cos(\alpha) - V_{iy} \sin(\alpha))^2}. \quad (38)$$

It is also convenient to define the “angle of incidence” β in the following way:

$$\beta = \arctan\left(\frac{V_{ix}}{V_{iy}}\right). \quad (39)$$

If the ions are strongly magnetized, one expects that $\beta \approx \alpha$. Close to the electrode, where the electric field is strong, the ions should move (almost) in the direction of the electric field, and this would imply $\beta \approx 90$ degrees—normal incidence of ions to the electrode.

III. RESULTS

From Fig. 2, one realizes that the integration of the systems (27)–(31) and/or (33)–(36) is started at a certain point,

which is set to zero, $X=0$. The integration then proceeds in the positive direction of X towards the electrode. The boundary values of the unknown functions at $X=0$ must be selected in order to solve this system of ordinary differential equations. When one is dealing with the system (27)–(31), the following boundary conditions are selected:

$$\begin{aligned} \Psi(0) &= 0, & V_{ix}(0) &= V_0, & V_{iy}(0) &= 0, \\ V_{iz}(0) &= 0, & N_i(0) &= 1, & \frac{d\Psi}{dX}(0) &= 0. \end{aligned} \quad (40)$$

For a system of five equations with five unknown functions, six boundary conditions are needed, since the Poisson Eq. (31) is of the second order. When the system (33)–(36) has to be solved, the boundary conditions are

$$\Psi(0) = 0, \quad V_{ix}(0) = V_0, \quad V_{iy}(0) = 0, \quad V_{iz}(0) = 0. \quad (41)$$

The physical arguments for such boundary conditions can be explained easily. The first boundary condition $\Psi(0)=0$ on one hand sets the potential at the initial point to zero and is also consistent with unit plasma density—see (3)—at $X=0$. At the starting point, there should also be no electric field and no directed ion flow. So, all velocity components should be zero. But, in this case, only the trivial solution of the systems (27)–(31) and (33)–(36) could be found. So, a small

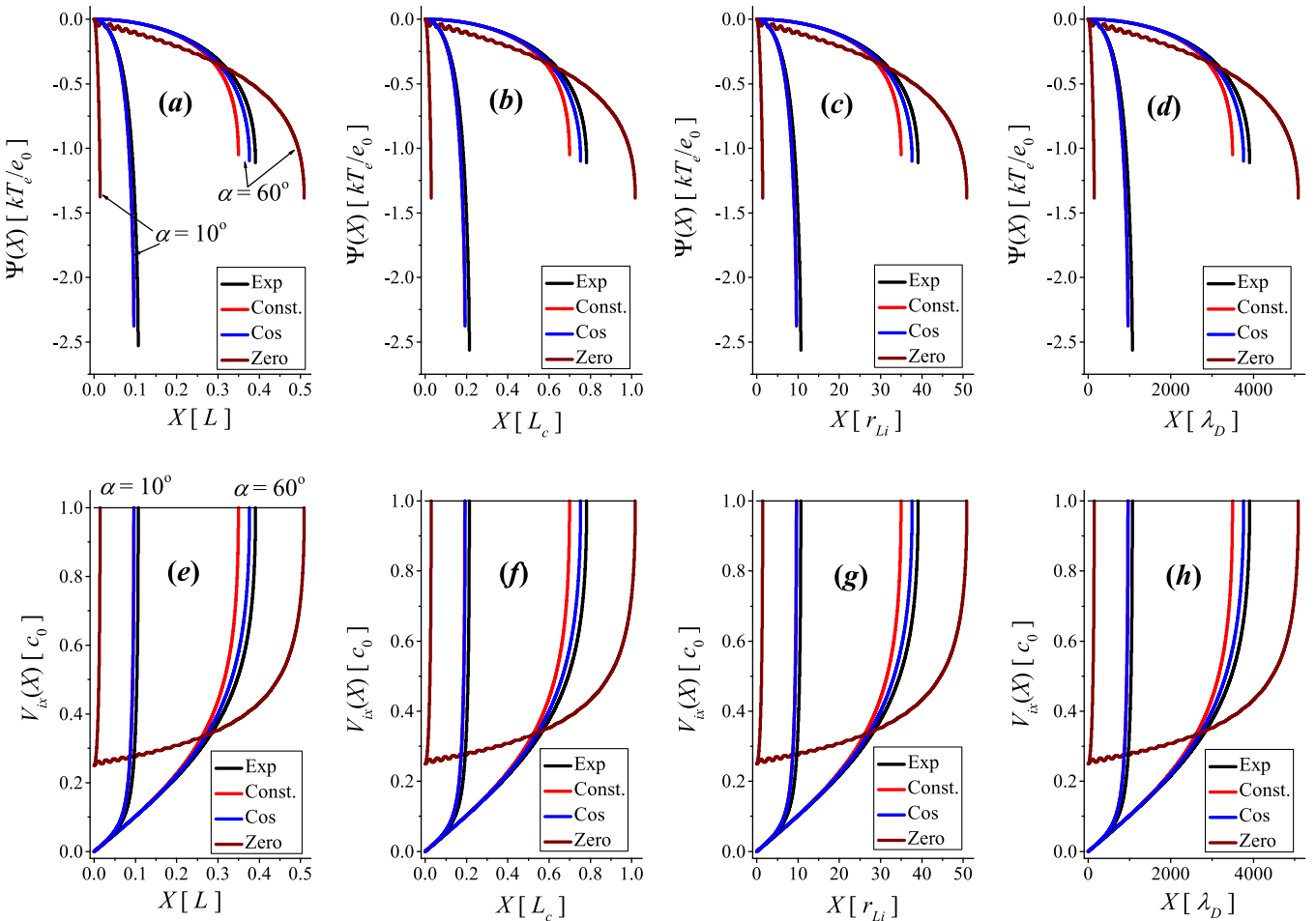


FIG. 3. An example of the solution of the system (33)–(36) for the parameters $K=100$, $Z=2$, $\varepsilon=10^{-4}$ and $\Theta=0$ and boundary conditions given by (41) with $V_0=10^{-8}$ for the constant (13), exponential (14), and cosine (15) source terms, while for the zero (12) source term, $V_0=0.25$ is selected. Four line colors correspond to four different source terms, as indicated by the legend in the plots.

initial ion velocity V_0 in the direction towards the electrode must be selected. A typical value selected in this work is $V_0 = 10^{-8}$.

Let us first take a look at an example of a solution of the system (33)–(36), shown in Fig. 3. The following parameters are selected: $K = 100$, $Z = 2$, $\varepsilon = 10^{-4}$, and $\Theta = 0$. Two values of α are selected, which are $\alpha = 10^\circ$ and $\alpha = 60^\circ$. The space coordinate is normalized to all 4 length scales: L , L_c , r_{Li} , and λ_D , and all four ion source terms (12), (13), (14), and (15) are used. The boundary conditions are given by (41). For the constant (13), exponential (14) and cosine (15) source term $V_0 = 10^{-8}$ are selected, while for the zero (12) source term, $V_0 = 0.25$ is taken. The curves that correspond to the solutions obtained with different source terms are given by a legend in the graphs. In the top plots (a)–(d), the potential profiles $\Psi(X)$ are shown, and in the bottom plots (e)–(h), the ion velocity profiles $V_{ix}(X)$ are displayed. The selection of the parameters is not motivated to model any specific experiment, but rather to keep the different length scales far apart in the sense that $L \sim L_c \gg r_{Li} \gg \lambda_D$. On one hand, we wish to keep the mean free path L_c and the ionization length L much larger than the Larmor radius r_{Li} , so that the magnetic field effects are not counteracted to much by ionizations and collisions. On the other hand, we also want to keep the Larmor radius r_{Li} much smaller than the Debye length λ_D so that the magnetic field effects and space charge effects can be clearly distinguished. Since the computational limitations set the lower boundary for ε at around $\varepsilon = 10^{-5}$ (see below—Figs. 6 and 7) there is not much freedom left for the selection of K and Z . From the values $K = 100$, $Z = 2$, and $\varepsilon = 10^{-4}$, it is easy to find using (22)–(24) that $L = 2L_c = 100r_{Li} = 10000\lambda_D$. As expected, the selection of the length-scale L , L_c , r_{Li} , or λ_D for the normalization of the space coordinate has no effect to the solutions of the system (33)–(36). The only effect is the expansion or stretching of the horizontal axis in the ratio determined by the values K , Z , and ε .

As the integration of the system (33)–(36) progresses in the positive direction of X , the velocity V_{ix} increases, while

the potential Ψ decreases. When V_{ix} reaches the ion sound velocity V_S , the system (33)–(36) becomes singular and the computation breaks down. This happens at the sheath edge, $X = X_{SE}$, and the respective potential is called the sheath edge potential Ψ_{SE} —see also Fig. 1. For $\Theta = 0$, the ion sound velocity is $V_S = 1$. As the integration progresses and V_{ix} approaches to V_S , smaller and smaller step ΔX must be taken for the computation. The computation is stopped when the difference $V_S - V_{ix}$ drops below 10^{-4} . Only two magnetic field angles α are shown in Fig. 3, but this is enough to illustrate the expected dependence of X_{SE} and Ψ_{SE} on α : as α increases, X_{SE} increases and Ψ_{SE} decreases (but increases by *absolute value!*). This occurs because steeper inclination of magnetic field impedes the motion of charged particles towards the collector. A larger electric field in the pre-sheath is then needed to accelerate the particles towards the electrode. This larger electric field results in a larger potential drop across the pre-sheath on a shorter distance. It can be noticed that there is a quantitative difference between the solutions that correspond to the zero source term (12) on one hand and the solutions that correspond to the other three source terms (13)–(15) on the other hand. There is a substantial difference in X_{SE} and Ψ_{SE} . But, most striking is the huge difference between $V_0 = 10^{-8}$ for the non-zero source terms (13), (14), and (15) on one hand and $V_0 = 0.25$ for the zero (12) source term on the other hand. In order to obtain a solution with the same order of magnitude of X_{SE} , the velocity V_0 must be increased for many orders of magnitude if any of the source terms (13)–(15) is replaced by the zero source term (12).

In order to illustrate the difference between the solutions obtained with the source terms (13)–(15) on one hand and with the source term (12) on the other, the dependence of the sheath edge X_{SE} on V_0 is presented in Fig. 4. The following parameters are selected: $K = 50$, $Z = 1$, $\alpha = 20^\circ$, and $\Theta = 0$. The ionization length L is selected for the normalization of the space coordinate. The system (33)–(36) is solved using the boundary conditions (41), where V_0 is gradually increased. At each V_0 , the coordinate X_{SE} , where the

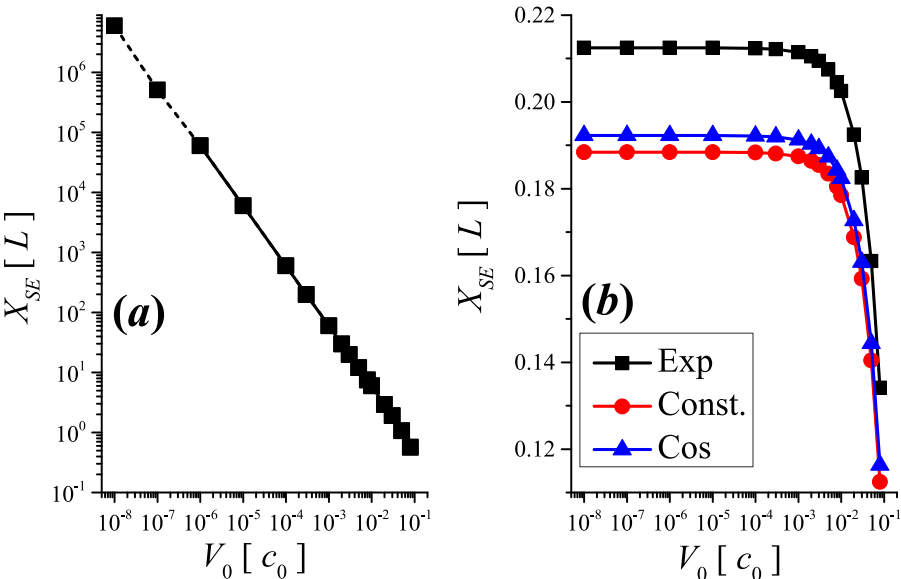


FIG. 4. The position X_{SE} versus V_0 found from the system (33)–(36), if the zero source term (12) is used is shown in plot (a). In plot (b), the same dependence is shown for the source terms (13)–(15). Plot (a) is displayed in the log-log scale, while plot (b) is shown in the semi-log scale. The parameters are: $K = 50$, $Z = 1$, $\alpha = 20^\circ$, and $\Theta = 0$. When the zero source term is used the computation is unreliable for $V_0 < 10^{-6}$, so the respective results are shown with the dashed line.

computation breaks down, is recorded. Results for the zero source term (12) are shown in plot (a). This graph is displayed in log-log scale. The velocity V_0 is increased over many orders of magnitude, and also X_{SE} varies over many orders of magnitude. The quantities V_0 and X_{SE} are roughly inversely proportional to one-another. For $V_0 < 10^{-6}$, the computation becomes unreliable, and consequently, the estimated values of X_{SE} for $V_0 < 10^{-6}$ are presented with the dashed line. Results for the other three source terms are presented in plot (b). The lines and symbols that correspond to different source terms are explained by a legend in the plot. For the source terms (13)–(15), there are no computational problems for the velocities V_0 in the region $10^{-8} < V_0 < 10^{-6}$. This graph is presented in semi-log scale. The velocity V_0 is increased over seven orders of magnitude, but the resulting X_{SE} drops only for about 50%. For V_0 between 10^{-8} and 10^{-4} , the sheath edge position X_{SE} is almost independent of V_0 . For larger values of V_0 , the value of X_{SE} starts to decrease with V_0 increasing.

A careful examination of the profiles obtained with the zero source term in Fig. 3 reveals another interesting difference between the solutions obtained with the source terms (13)–(15) on one hand and with the source term (12) on the other. The potential and velocity profiles obtained with the zero source term at $\alpha = 60^\circ$ exhibit oscillations that do not have a large amplitude but they can be seen clearly. If the collision rate Z is decreased, the oscillations become

stronger. An example is shown in Fig. 5. The system (33)–(36) is solved using the zero source term (12) and the boundary conditions (41), with $V_0 = 0.1588$. The parameters are: $K = 50$, $Z = 0.001$, $\alpha = 20^\circ$, and $\Theta = 0$. In plot (a), the potential profile $\Psi(X)$ is presented; in graph (b), the density profile, $\exp(\Psi(X))$, is displayed; in figure (c), the angle of incidence $\beta(X)$ (formula (39)) is shown; and in plots (d), (e), and (f), the velocity profiles $V_{ix}(X)$, $V_{iy}(X)$, and $V_{iz}(X)$ are displayed. Large amplitude oscillations can be observed. Somewhat similar oscillating solutions for the ion density profiles have been found also by Masoudi¹⁷ and Zou *et al.*⁴⁶ The amplitude of the oscillations of the velocity $V_{iy}(X)$ even exceeds the ion sound velocity. In the coordinate system shown in Fig. 2, the direction of z axis is the direction of the $\mathbf{E} \times \mathbf{B}$ drift. The velocity V_{iz} exhibits symmetric oscillations around zero value. The amplitude and period of the observed oscillations exhibit parametric dependence on magnetic field density K , magnetic field angle α , collision rate Z , and velocity V_0 . A systematic study would require a separate investigation, which is beyond the scope of this work. Let us only add that the solutions of the system (27)–(31) also exhibit very similar oscillations at the same parameters. It should be emphasized that no such oscillations have been found with the source terms (13)–(15). From the results shown in Figs. 3–5, it is clear that the solutions of the systems (27)–(31) and (33)–(36) obtained with the zero source term (12) on one hand and with the source terms (13)–(15) on the other exhibit

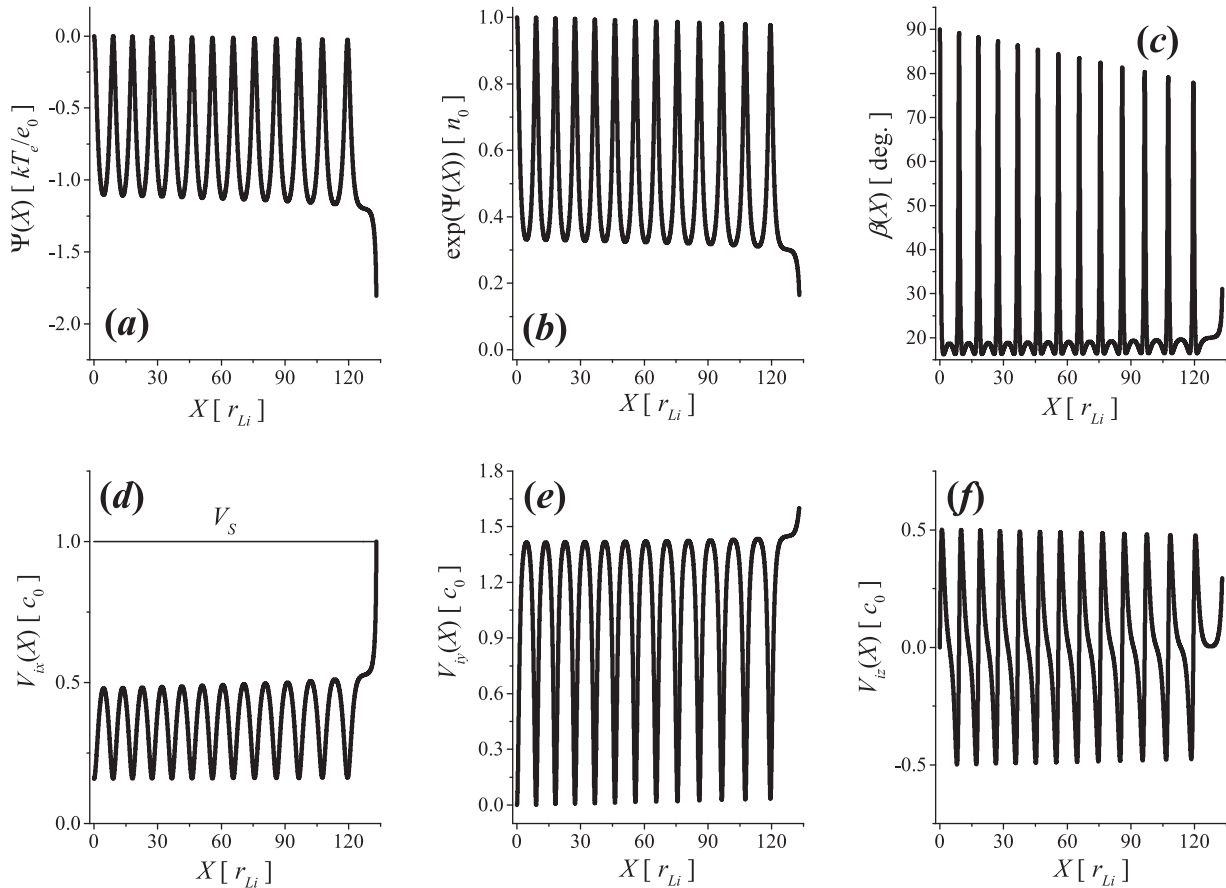


FIG. 5. A solution of the systems of Eqs. (33)–(36) using the zero source term (12), the parameters: $K = 50$, $Z = 0.001$, $\alpha = 20^\circ$, and $\Theta = 0$ and the boundary conditions (41), with $V_0 = 0.1588$.

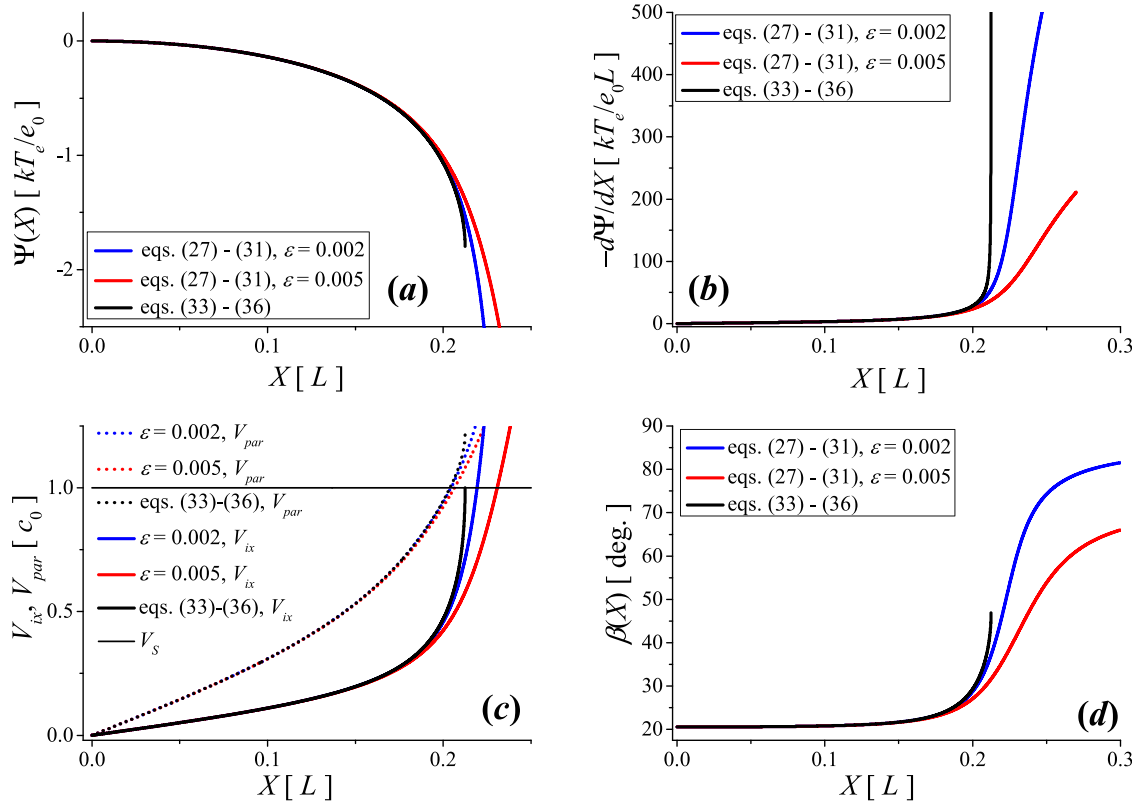


FIG. 6. Solutions of the systems (33)–(36) and (27)–(31). In plot (a), the potential profiles $\Psi(X)$ are presented; in graph (b), the electric field profiles $-d\Psi/dX$ are shown; in figure (c), the velocity profiles $V_{ix}(X)$ (solid lines) and $V_{par}(X)$ (dotted lines) are displayed; and in plot (d), the profiles of the angle of incidence $\beta(X)$ are presented. For the system (33)–(36), the parameters are: $K = 50$, $Z = 1$, $\alpha = 20^\circ$, and $\Theta = 0$. For the system (27)–(31), the same parameters are selected with addition of 2 values of ε , $\varepsilon = 0.002$, and $\varepsilon = 0.005$. Lines that correspond to particular solutions are given by the legends in the plots.

large differences. One very obvious difference is strong sensitivity of the solutions of the systems (27)–(31) and (33)–(36) on V_0 , when the zero source term (12) is selected. The second difference are oscillatory solutions of the systems (27)–(31) and (33)–(36), which are found very often, when the source term (12) is used, but are not observed, when the source terms (13)–(15) are used.

As it is shown in Sec. IV, the assumption of the Boltzmann relation for the electrons, implies that there is no mechanism for creation or annihilation of the electrons. Since there cannot be a physical mechanism, where only positive ions and not also electrons would be created and annihilated, the model, which uses the Boltzmann relation for the electrons and $S_i \neq 0$ for the ions, is not self-consistent. Nevertheless, such model has been used extensively^{3,8,9,18,22,23,32,33,35,42,44} for the analysis of magnetized plasma-wall transition by many authors. A possible reason for this could be the above mentioned problems related to the use of the zero source term (12) and the fact that the authors were probably not aware of the inconsistency that is introduced into the model in this way.

Let us now take a look at an example of the solution of the systems (27)–(31) and (33)–(36) together—Fig. 6. For the system (33)–(36), the following parameters are selected: $K = 50$, $Z = 1$, $\alpha = 20^\circ$, and $\Theta = 0$. The exponential source term (14) is selected, and the space coordinate is normalized to the ionization length L . The boundary conditions (41) are taken with $V_0 = 10^{-8}$. If the space coordinate is not normalized to the Debye length λ_D , the system (33)–(36) does not

depend on ε . At the sheath edge X_{SE} , where V_{ix} reaches the ion sound velocity V_s —thin black solid line in plot (c), the system (33)–(36) becomes singular and the computation breaks down. The condition $V_{ix}(X_{SE}) = V_s$ is in fact the well known Bohm criterion. Close to this point, the electric field $-d\Psi/dX$ —black line in plot (b)—increases very steeply. In graph (d), the profiles $\beta(X)$ of the angle of incidence (formula (39)) are shown. The black line shows the solution of the system (33)–(36). It can be seen very well how close to the sheath edge the ion motion is deviated from the direction along the magnetic-field lines in the direction of the electric field. In graph (c), the velocity V_{ix} is shown in solid black line and the corresponding parallel part of the velocity V_{par} (formula (37)) in black dotted line. The parallel velocity V_{par} reaches the ion sound velocity V_s at X_{MSE} —the magnetized pre-sheath edge. The condition $V_{par}(X_{MSE}) = V_s$ is sometimes called the Bohm-Chodura criterion.^{30,40} The respective potential is the magnetized pre-sheath edge potential Ψ_{MSE} . The region between X_{MSE} and X_{SE} is called the Chodura layer—see also Fig. 1. From the comparison of the graphs (c) and (d), it can be seen that the deviation of ion motion away from the direction of the magnetic field indeed starts in this layer. The system (27)–(31) on the other hand depends on ε , no matter which length scale is selected for the normalization of the space coordinate. In Fig. 6, two values of ε are selected, $\varepsilon = 0.002$ and $\varepsilon = 0.005$, while the other parameters are not changed. The boundary conditions are given by (40) with $V_0 = 10^{-8}$. Different line colors are used for different values of ε according to the legend shown in the figure. In

plot (c), solid lines show V_{ix} , while the dotted lines represent V_{par} . The difference between the solutions of the system (33)–(36) on one hand and of the system (27)–(31) on the other hand is quite obvious. From $K=50$ and $\varepsilon=0.005$, one finds easily using the formulas (22)–(24) that $r_{Li}/\lambda_D=4$, while for $\varepsilon=0.002$, one gets $r_{Li}/\lambda_D=10$. Because the Larmor radius and the Debye length are so close to one-another, the plasma described by the parameters $K=50$, $Z=1$, $\alpha=20^\circ$, $\Theta=0$, and $\varepsilon=0.005$ or $\varepsilon=0.002$ is strongly magnetized. The effect of this strong magnetic field can be best seen in the profiles of the angle of incidence $\beta(X)$ —Fig. 6(d). As the ions penetrate deeper and deeper into the sheath, their motion is only slowly deviated into the direction of the electric field lines—that is, perpendicular to the collector. Another important difference between the solutions of the system (33)–(36) on one hand and of the system (27)–(31) on the other hand is the following. When the system (27)–(31) is integrated, the computation does not break down, when the sheath edge X_{SE} is reached, i.e., when $V_{ix}=V_S$. Instead, the computation can be continued to arbitrary value of X .

The results shown in Fig. 6 are in very good agreement with the so called asymptotic two-scale limit,⁵⁰ which is

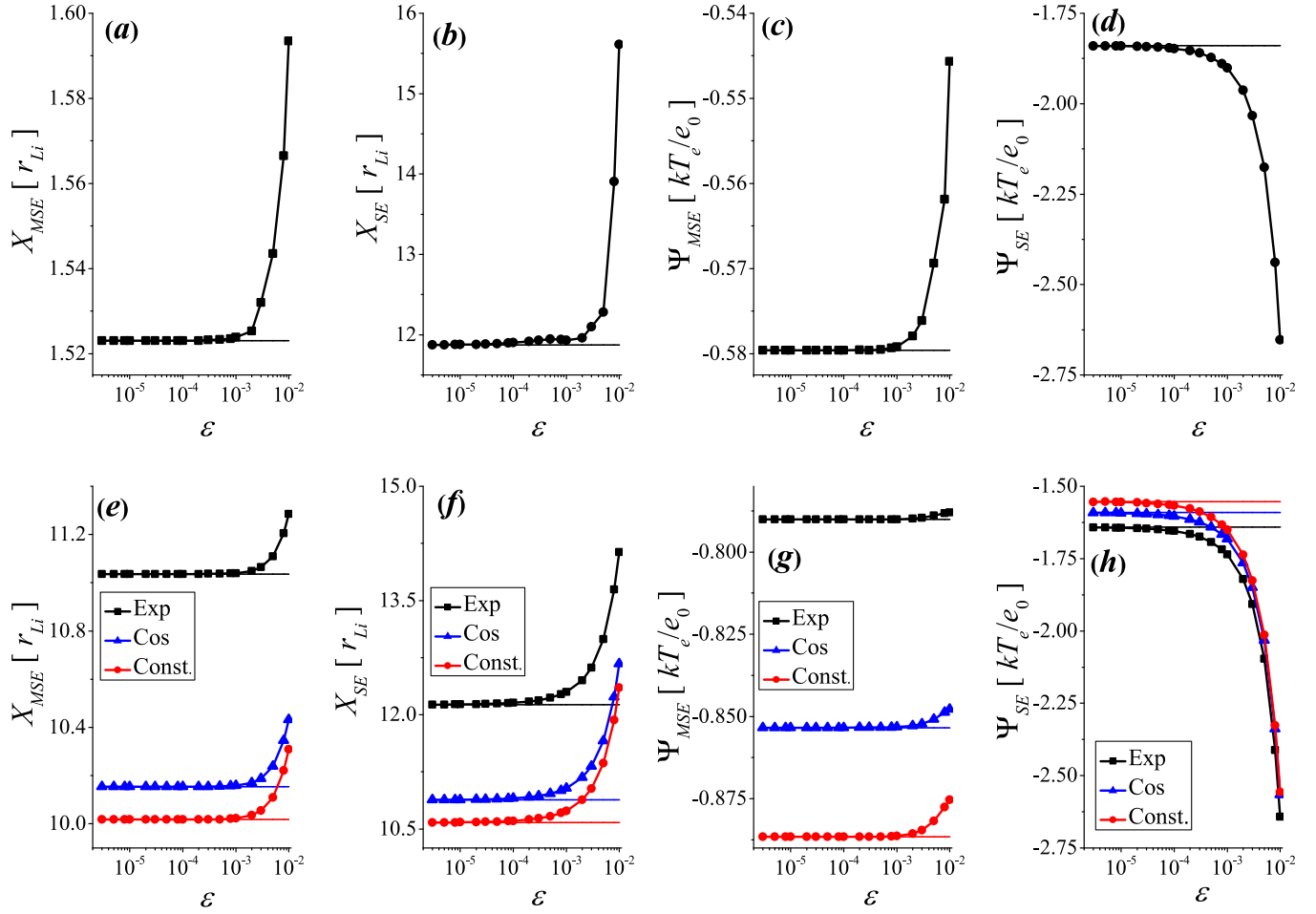


FIG. 7. The solutions of the system (27)–(31) versus ε . The parameters are: $K=50$, $Z=0.01$, $\alpha=20^\circ$, and $\Theta=0$. In the top plots (a)–(d), solutions obtained with the zero source term (12) and boundary conditions (40) with $V_0=0.158941$ are shown. In the bottom plots (e)–(h), solutions obtained with the source terms (13)–(15) and boundary conditions (40) with $V_0=10^{-8}$ are displayed. Lines and symbols that correspond to each of the source terms (13)–(15) are labeled by a legend in the plots. Thin solid lines indicate the respective solutions of the system (27)–(31), which are independent of ε . In graph (b), a part of plot (a) is shown on an expanded scale, and in figure (d), a part of graph (c) is plotted on an expanded scale.

obtained, when $\varepsilon \rightarrow 0$. If the space coordinate is normalized to L or L_c or r_{Li} and $\varepsilon \rightarrow 0$ is inserted, then $A_3 \rightarrow 0$ (Table I). If L_c or r_{Li} are used for the normalization of the space coordinate, the collision rate Z and the magnetic field K must be low enough that $A_3 = \varepsilon^2 Z^2 \rightarrow 0$ or $A_3 = \varepsilon^2 K^2 \rightarrow 0$. In this case, Poisson Eq. (31) becomes the neutrality condition (32) and the system (27)–(31) is transformed into (33)–(36). The plasma-sheath problem is then treated in the so called pre-sheath scale of the asymptotic two-scale limit. In this scale, the sheath edge is characterized by the electric field singularity—see Refs. 50 and 51 and references therein. Numerical solution of the system (33)–(36) indeed exhibits very strong jump of the electric field $-d\Psi/dX$ at the sheath edge, and then the solution breaks down. As already mentioned, the step ΔX is decreased as the integration approaches to the sheath edge and is stopped at a certain distance before the exact value of sheath edge. Because of that the electric field $-d\Psi/dX$ found from the numerical solution of the system (33)–(36) has a finite value at the “sheath edge.”

For a finite ε , the system (27)–(31) is solved in the pre-sheath and in the sheath region at the same time. The results displayed in Fig. 6 show that as ε is decreased, the profiles found from the solutions of the system (27)–(31) in the pre-

sheath region approach to the solutions obtained from the system (33)–(36) as long as the parameters K , Z , α , Θ , and also boundary conditions are the same for both systems. This is illustrated additionally in Fig. 7. The following parameters are selected: $K = 50$, $Z = 0.01$, $\alpha = 20^\circ$, and $\Theta = 0$, while ε is gradually increased. Every time the systems of Eqs. (27)–(31) and (33)–(36) are solved using the boundary conditions (40) or (41). For the source terms (13)–(15), $V_0 = 10^{-8}$ is selected, while for the zero source term (12), $V_0 = 0.158941$ is taken. The space coordinate is normalized to the Larmor radius r_{Li} . Every time the values of X_{MSE} , X_{SE} , Ψ_{MSE} , and Ψ_{SE} are recorded and plotted versus ε . The values of ε go from $\varepsilon = 3 \cdot 10^{-6}$ to $\varepsilon = 0.01$. As ε is decreased, the electric field profile close to the sheath edge becomes steeper and steeper, and consequently, also the integration step size ΔX has to be decreased. This makes the computation more and more time consuming. For the values of ε below 10^{-5} , the computation time becomes unacceptably long. On the other hand, ε can also not be increased arbitrarily. For ε larger than 0.024, the system (27)–(31) becomes stiff and cannot be solved any more. At $K = 50$ and $\varepsilon = 0.024$, the ratio $\lambda_D/r_{Li} = 1.2$; this means that Larmor radius is smaller than the Debye length. As ε is decreased, the values of X_{MSE} , X_{SE} , Ψ_{MSE} , and Ψ_{SE} found from the system (27)–(31) approach to the solutions obtained from the system (33)–(36). Already, at approximately $\varepsilon \sim 10^{-4}$, the difference is negligibly small. In the bottom plots (e)–(h), results for the non-zero source terms (13)–(15) are shown. The obtained values of X_{MSE} , X_{SE} , Ψ_{MSE} , and Ψ_{SE} that correspond to the three non-zero source terms are rather close together. The dependence of X_{MSE} , X_{SE} , Ψ_{MSE} , and Ψ_{SE} on ε obtained when the zero source term is used is presented in the top graphs (a)–(d) in Fig. 7. Qualitative dependence X_{MSE} , X_{SE} , Ψ_{MSE} , and Ψ_{SE} on ε is similar to the case when the non-zero source terms are used, but any quantitative comparison between the results shown in the plots (a)–(d) on one hand and in the graphs (e)–(h) on the other makes no sense. A somewhat peculiar value $V_0 = 0.158941$ for the zero source term is selected in order to get the values of X_{SE} obtained by all four source terms as close together as possible.

As shown in Fig. 6, the integration of the system (27)–(31) can be continued to arbitrary X . A question arises where to stop it. A very natural selection is the floating potential Ψ_f . This is the potential where the ion and electron fluxes are equal. The ion flux $J_i(X)$ can be found easily. Once the system (27)–(31) or (33)–(36) is solved and the ion density $N_i(X)$ and the ion velocity $V_{ix}(X)$ profiles are found, the ion flux is obtained simply from:

$$J_i(X) = N_i(X)V_{ix}(X). \quad (42)$$

The electron flux j_e to the collector can be estimated in a similar way as in, e.g., Ref. 44. In our simple one dimensional model, the electron velocity distribution function is assumed to be a cut-off Maxwellian given by

$$f_{e0}(v_x) \simeq n_0 \sqrt{\frac{m_e}{2\pi kT_e}} \exp\left(-\frac{m_e v_x^2}{2kT_e}\right) H(v_x + v_c). \quad (43)$$

Here, v_c is the cut-off velocity, given by (44) below, and the sign \simeq tends to an equals sign, as Φ_f approaches to zero. The potential profile is such (see Fig. 1) that the potential is zero at $x = 0$ and then decreases monotonically in the positive x direction towards the electrode. So, only those electrons that have the velocity v_x larger than v_c can move towards the electrode, while slower electrons are repelled in the opposite direction. If the absolute value of the collector potential is Φ_f , only those electrons, that have the velocity v_x in the direction towards the collector larger than v_c , given by

$$v_c = \sqrt{\frac{2e_0 \Phi_f}{m_e}}, \quad (44)$$

can reach the collector and contribute to the current. The electron flux to the collector is therefore found from

$$\begin{aligned} j_e &= \int_{-\infty}^{\infty} v_x f_{e0}(v_x) dv_x = n_0 \sqrt{\frac{m_e}{2\pi kT_e}} \int_{v_c}^{\infty} v_x \exp\left(-\frac{m_e v_x^2}{2kT_e}\right) dv_x \\ &= n_0 \sqrt{\frac{kT_e}{2\pi m_e}} \exp\left(-\frac{e_0 \Phi_f}{kT_e}\right), \end{aligned} \quad (45)$$

where (44) has been taken into account. Using (22)–(24), the normalized electron flux J_e , given in the units $n_0 c_0$, is written as

$$J_e(\Psi_f) = \frac{j_e}{n_0 c_0} = \frac{1}{\sqrt{2\pi\mu}} \exp(\Psi_f), \quad (46)$$

where

$$\Psi_f = -\frac{e_0 \Phi_f}{kT_e}.$$

The floating potential Ψ_f is then found from

$$N_i(X_f) V_{ix}(X_f) = \frac{1}{\sqrt{2\pi\mu}} \exp(\Psi_f), \quad \Psi_f \equiv \Psi(X_f). \quad (47)$$

Once the system (27)–(31) is solved and the ion density $N_i(X)$, the ion velocity $V_{ix}(X)$, and the potential $\Psi(X)$ profiles are found, the floating potential Ψ_f and the respective position X_f where Eq. (47) is fulfilled can be found easily.

An example of the determination of the floating potential is illustrated in Fig. 8. The following parameters are selected: $K = 50$, $Z = 2$, $\alpha = 20^\circ$, $\mu = 1/25$, $\varepsilon = 10^{-5}$, and $\Theta = 0$. The system (27)–(31) is solved four times using all four ion source terms (12)–(15). The space coordinate is normalized to the ionization length L . Once the potential $\Psi(X)$, ion density $N_i(X)$, and ion velocity $V_{ix}(X)$ profiles are found, the ion $J_i(X)$ and electron $J_e(X)$ profiles can be found easily. They are shown in plots (b) and (c). The electron to ion mass ratio μ is taken very large $-1/25$ —in order to keep the electron flux so small that it can be compared to the ion flux in the same graph—graph (b). In graph (c), a part of Fig. (b) is shown on an expanded scale. The position X_f , where the intersection of the curves $J_i(X)$ and $J_e(X)$ is found, is recorded. Then the respective floating potential is found in graph (e), where the potential $\Psi(X)$ profiles are shown. If the

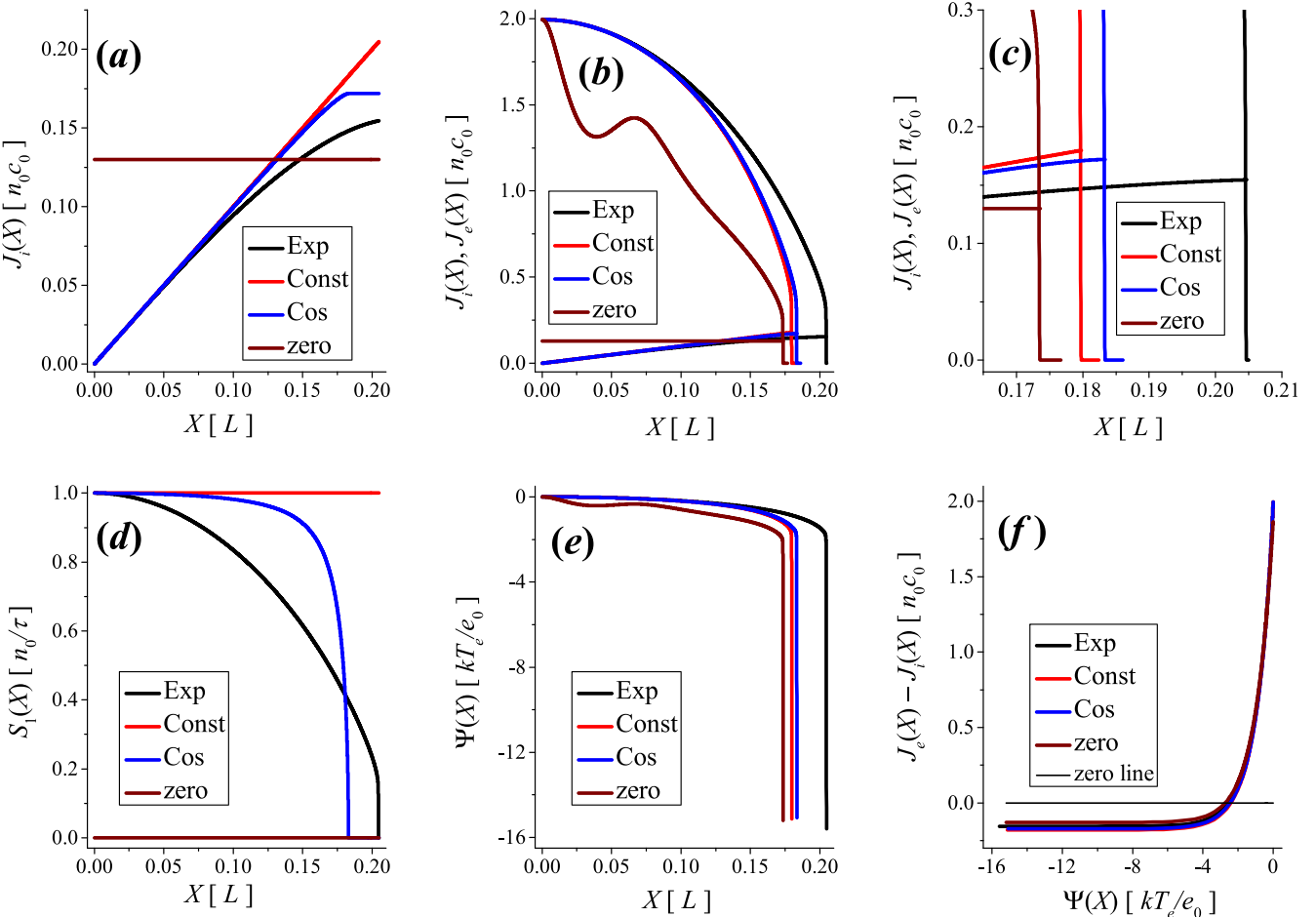


FIG. 8. Ion fluxes $J_i(X)$ —(a), electron $J_e(X)$ and ion $J_i(X)$ fluxes—(b), a part of plot (b) on an expanded scale—(c), profiles of the source terms $S_1(X)$ —(d), potential profiles $\Psi(X)$ —(e), and current voltage characteristics of the collector $J_e(x) - J_i(x)$ versus $\Psi(X)$ —(f). The parameters are $K = 50$, $Z = 2$, $\alpha = 20^\circ$, $\varepsilon = 10^{-5}$, $\mu = 1/25$, and $\Theta = 0$. The system (27)–(31) is solved for all 4 source terms (12)–(15)—see legend in the plots. The space coordinate is normalized to the ionization length L .

difference of the electron and ion fluxes $J_e(X) - J_i(X)$ is plotted versus the potential $\Psi(X)$, the current voltage characteristic of the collector can be obtained. It is displayed in graph (f). The intersection of the curve $J_e(X) - J_i(X)$ with the zero line gives the floating potential Φ_f . In plot (a), the ion fluxes $J_i(X)$ that correspond to the four source terms are plotted in the full scale, and in graph (d) below, the profiles of the respective sources $S_1(X)$ are displayed. According to Eq. (27), the ion source term $S_1(X)$ is a derivative of the ion flux $J_i(X)$. For the zero and constant source terms, this can be seen easily. For the cosine and the exponential source term, their dependence on X can be found only after the system (27)–(31) has been solved and the profiles of the potential $\Psi(X)$, ion density $N_i(X)$, and ion velocity $V_{ix}(X)$ have been obtained. The same is true also for the ion fluxes $J_i(X)$. From graphs (a) and (d), it can be seen that the ion fluxes and the source terms are consistent with the Eq. (27). In this way, the quality of the numerical solution of the system (27)–(31) is tested.

In Fig. 9, the effect of the ion temperature Θ to the solutions of the system (33)–(36) is illustrated. The parameters are the following: $K = 50$, $Z = 2$, and $\alpha = 20^\circ$, and three values of Θ are selected. The space coordinate is normalized to the ionization length L . The boundary conditions are given

by (41), with $V_0 = 10^{-8}$ for the non-zero source terms (13)–(15) and $V_0 = 0.14$ for the zero source term (12). The potential profiles $\Psi(X)$ are shown in the left plots (a) and (c), while the velocity profiles $V_{ix}(X)$ are displayed in the right plots (b) and (d). With an increase in Θ , the ion sound velocity $V_S = \sqrt{1 + \Theta}$ also increases. Because of that, also the pre-sheath length increases. For the zero source term, the variation of the pre-sheath length with ion temperature is much larger than for the non-zero source terms. The potential and velocity profiles obtained with the zero source term exhibit oscillations—they are not monotonic—while the profiles obtained with the non-zero source terms (13)–(15) are monotonic.

If one attempts to solve the system (27)–(31) with $\Theta > 0$, it turns out that V_0 must be increased considerably. For a too small velocity V_0 , the system (27)–(31) is stiff and no numerical solution can be found. In Fig. 10, the minimum value of V_0 where the solution of the system (27)–(31) can be found is plotted versus the ion temperature Θ . This velocity is called the critical ion velocity V_{0c} , or just critical velocity. The following parameters are selected: $K = 50$, $Z = 2$, $\alpha = 20^\circ$, and $\varepsilon = 10^{-4}$. The exponential source term (14) is used. For the zero (12), the constant (13), and the cosine (15) source terms, the results are almost identical, and they are

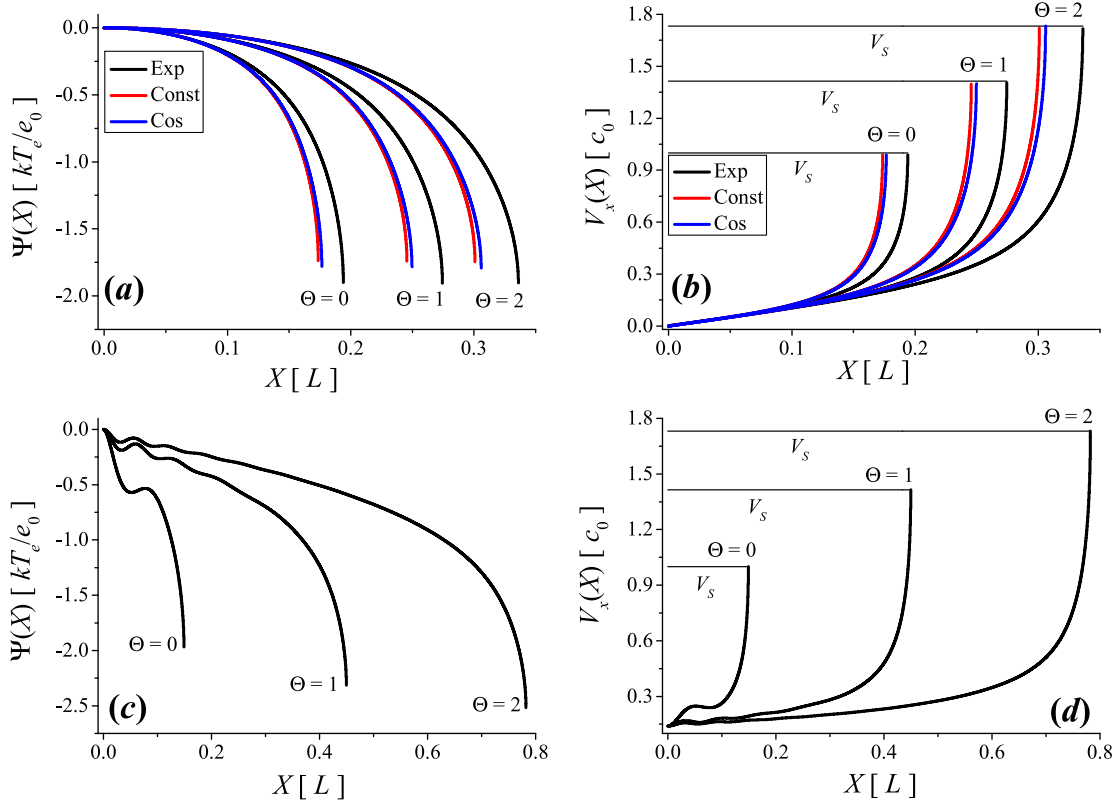


FIG. 9. Potential $\Psi(X)$ and velocity $V_{ix}(X)$ profiles found from (33)–(36) for the parameters $K = 50$, $Z = 2$, $\alpha = 20^\circ$, and 3 values of Θ . The boundary conditions are given by (41), with $V_0 = 10^{-8}$ for the source terms (13)–(15)—plots (a) and (b)—and $V_0 = 0.14$ for the zero source term (12)—graphs (c) and (d).

not shown. From Fig. 10, it can be seen that the critical velocity V_{0c} is slightly larger than $\sqrt{\Theta}$. Similar observation has been made also by Yasserian and Aslaninejad.³⁵ From (22)–(24), it can be seen easily that $V_{0c} \sim \sqrt{\Theta}$ corresponds to the ion thermal velocity $\sqrt{kT_i/m_i}$.

In relation to the results shown in Fig. 10, another remark should be given about the use of the zero source term (12). As Θ decreases, also V_{0c} must be decreased. When Θ drops to approximately 0.001 and the respective V_{0c} is around 0.0317, the system (27)–(31) becomes very difficult

to solve, because the pre-sheath length increases strongly. The situation is similar, as illustrated in Fig. 4, where the system (33)–(36) has been solved with $\Theta = 0$. The system (27)–(31) with $\Theta > 0$ is even more sensitive to the choice of V_0 , and considerable numerical problems arise already at higher values of V_0 than in the case of zero ion temperature.

If one wants to find the dependence of a certain parameter on Θ , one is faced with the following problem. As Θ is increased, also V_0 must be increased in order to solve the system (27)–(31). One possibility is to use the critical V_{0c} for

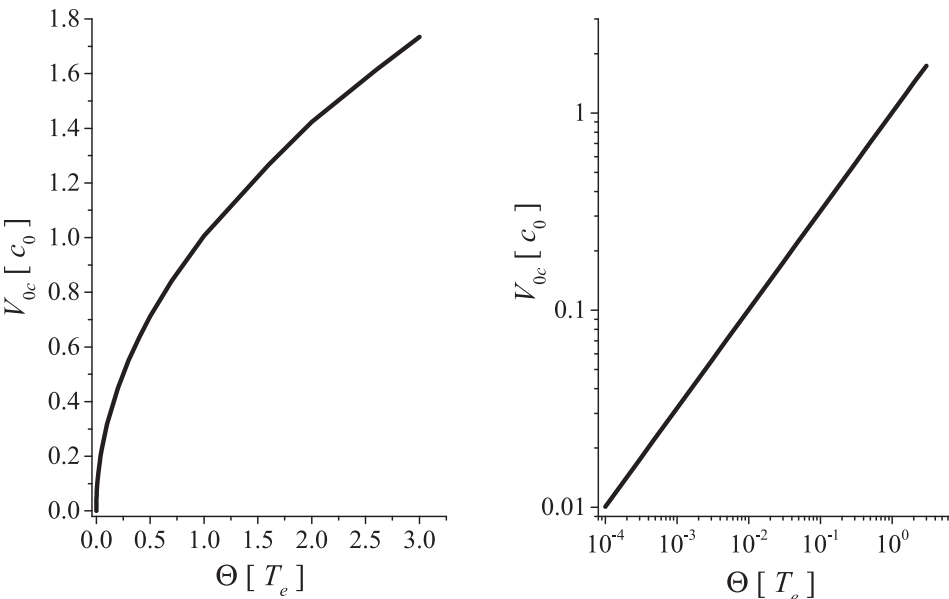


FIG. 10. Minimum (critical) velocity V_{0c} , at which a numerical solution of the system (27)–(31) can be found, versus the ion temperature Θ . In the left plot, both axis have linear scale, while in the right figure, the axis are in the logarithmic scale. The exponential source term (14) is used, the parameters are: $K = 50$, $Z = 2$, $\alpha = 20^\circ$, and $\varepsilon = 10^{-4}$.

each corresponding Θ and solve the system (27)–(31). Such solutions are, of course, difficult to compare, since each solution has been obtained with a different boundary condition. The other possibility is to use the largest velocity V_{0c} , which corresponds to the largest Θ also for all other smaller values of Θ . Such approach has an obvious problem. Let us assume that one wants to find the dependence of certain quantity on Θ in the range between $\Theta = 0$ and $\Theta = 2$. For $\Theta = 2$, $K = 50$, $Z = 2$, $\alpha = 20^\circ$, and $\varepsilon = 10^{-5}$, the critical velocity is $V_{0c} = 1.417$. This value is obviously above the ion sound velocity $V_S = \sqrt{1 + \Theta}$ for the values of Θ below 1. Using a velocity which is subsonic for some parameters and supersonic for other parameters as boundary condition obviously raises serious questions about the consistency of such an approach. Because of this, we propose another approach that we call the *critical ion velocity method*. It consists of the following:

- Select the parameters K , Z , ε , Θ , α , and μ and start the integration of the system (33)–(36) using the boundary conditions (41) with V_0 as small as possible. For the non-zero source terms (13)–(15), V_0 between 10^{-8} and 10^{-6} is appropriate, while for the zero source term (12), much larger values have to be selected, but, of course, below $\sqrt{\Theta}$.
- Continue the integration of the system (33)–(36) until V_{ix} reaches the critical value V_{0c} , which is required for the solution of the system (27)–(31) and record the values of the

potential, density, electric field, and velocity components in this point.

- Use the values obtained in the previous step as the boundary conditions (40) for the system (27)–(31) and solve it for $\Psi(X)$, $N_i(X)$, $V_{ix}(X)$, $V_{iy}(X)$ and $V_{iz}(X)$.

In Fig. 11, the critical ion velocity method is illustrated. The following parameters are selected: $K = 50$, $\alpha = 20^\circ$, $Z = 1$, and $\Theta = 0.01$. The system (33)–(36) is solved numerically using the boundary conditions (41), with $V_0 = 10^{-8}$. The exponential source term (14) is selected, and the space coordinate is normalized to the discharge length L . The integration of the system (33)–(36) is continued until the singularity is reached, when V_{ix} reaches the ion sound velocity $V_S = \sqrt{1 + \Theta} = 1.00498$. For $\Theta = 0.01$, the critical velocity is found to be $V_{0c} = 0.100098$ and V_{ix} reaches this value at $X_c = 0.09248$. The values of the parameters in this point are $\Psi(X_c) = -0.11575$, $N_i(X_c) = 0.890699$, $d\Psi/dX(X_c) = 2.75383$, $V_{iy}(X_c) = 0.263918$, and $V_{iz}(X_c) = 0.0519573$. These values are used as boundary conditions in (40), and the system (27)–(31) is then integrated. The obtained profiles depend on ε . Smaller ε means better precision because one discharge length L then contains larger number of Debye lengths λ_D . In Fig. 11, rather large values $\varepsilon = 0.005$ and $\varepsilon = 0.002$ are used for illustration purposes. For larger ε , the system (27)–(31) becomes stiff. The solid black line shows the solution of the system (33)–(36) in the region between 0 and X_c . The dotted

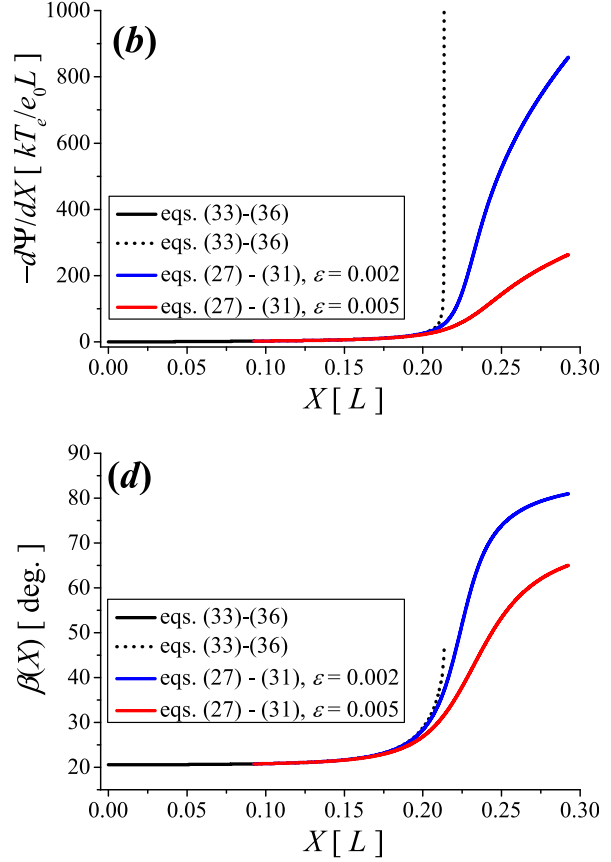
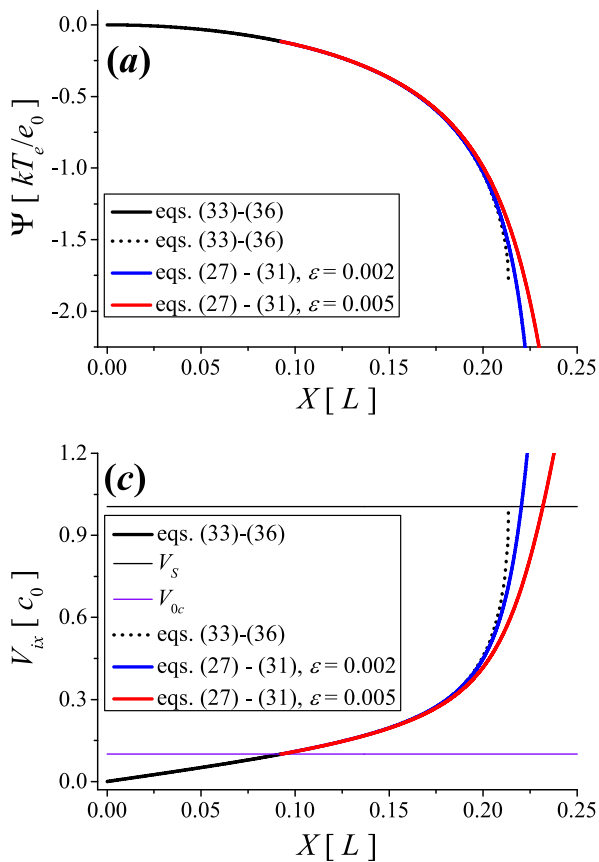


FIG. 11. Illustration of the critical ion velocity method. The parameters are: $K = 50$, $\alpha = 20^\circ$, $Z = 1$, and $\Theta = 0.01$. The critical velocity is $V_{0c} = 0.100098$, and ion sound velocity is $V_S = \sqrt{1 + \Theta} = 1.00498$. The solid black line shows the solution of the system (33)–(36) in the region between 0 and X_c . The dotted black line shows the solution of the system (33)–(36) in the region between X_c and X_{SE} . The solution of the system (27)–(31) is shown for $\varepsilon = 0.005$ and for $\varepsilon = 0.002$ with different line colors with the corresponding legend shown in the graphs.

black line shows the solution of the system (33)–(36) in the region between X_c and X_{SE} . The red line shows the solution of the system (27)–(31) for $\varepsilon=0.005$, and the blue line displays the solution of the system (27)–(31) for $\varepsilon=0.002$.

Some authors^{19–24,37} have studied the effects of finite ion temperature to the sheath in an oblique magnetic field using similar fluid model like ours. In majority of above mentioned papers, the problem is treated on the sheath scale of the asymptotic two-scale limit.⁵⁰ The sheath scale of the asymptotic two-scale limit is the second scale of the two-scale limit mentioned earlier in relation to Fig. 6. The sheath scale of the asymptotic two-scale limit is obtained when the space coordinate is normalized to the Debye length λ_D , and the limit $\varepsilon \rightarrow 0$ is taken. In this case, one gets (see Table I) $A_3=1$ and $A_1 \rightarrow 0$. If the magnetic field K is very large, then $A_2=\varepsilon K$ is finite, otherwise the magnetic field effects inside the sheath are negligible. In the sheath scale of the asymptotic two scale limit, the electric field at the sheath edge is zero, the ion flow at the sheath edge must fulfill the Bohm criterion, and at the sheath edge, the plasma is assumed to be neutral.⁵⁰ The approach taken by the authors in the above mentioned papers^{19–24} and also some others^{45,46} can therefore be summarized as follows. From the basic equations of the type (1)–(4) and an equation of state (e.g., (9)), a system of equations very similar to our system (27)–(31) is derived. Usually, some form of the Bohm criterion is also derived. The system of equations equivalent to our system (27)–(31) is then solved numerically. The boundary conditions at the sheath edge are formulated based on the assumption that the plasma at the sheath edge is neutral, which gives $N_i(0)=1$. Further, it is assumed that the electric field at the sheath edge is zero, $d\Psi/dX(0)=0$, the sheath edge potential is set to zero, $\Psi(0)=0$, and the Bohm criterion is fulfilled at the sheath edge, $V_{ix}(0)=V_S$. This is obviously equivalent to taking the boundary conditions (40), with $V_0=V_S=\sqrt{1+\Theta}$. In this work, we call the above described approach the KGG method after Khoramabadi, Ghomi, and Ghoranneviss, the authors of Ref. 19, although also other authors^{21–24} have used similar method. But Ghomi and Khoramabadi⁵² have presented a good argumentation for the use of such a method in non-magnetized plasma.

An example of the comparison of the critical ion velocity method and the KGG method is shown in Fig. 12. The following parameters are selected: $K=500$, $\alpha=20^\circ$, $Z=2$, $\Theta=2$, $\mu=1/3670.48$ (deuterium mass), and $\varepsilon=10^{-5}$. In plot (a), the potential profile $\Psi(X)$ is presented; in graph (b), the density profiles $N_i(X)$ for the ions and $\exp(\Psi(X))$ for the electrons are shown; and in figure (c), the ion and electron flux profiles $J_i(X)$ and $J_e(X)$ are displayed. These profiles are obtained from the system (27)–(31) using boundary conditions (41) with $V_0=V_S=\sqrt{1+\Theta}$. The exponential source term (14) is used, and the space coordinate x is normalized to the Debye length λ_D . From plots (a) and (c), the floating potential is found to be $\Psi_f=-2.64096$, while the respective coordinate is $X_f=20.35$. Since $X_{SE}=0$, this is also the sheath thickness and Ψ_f gives the sheath potential drop. In the bottom graphs (d)–(f) of Fig. 12, similar profiles are presented; only they are found with the critical ion velocity method, described above. Exactly, the same parameters are taken:

$K=500$, $\alpha=20^\circ$, $Z=2$, $\Theta=2$, $\mu=1/3670.48$, and $\varepsilon=10^{-5}$. The critical velocity is $V_{0c}=1.417$ and is reached at $X_c=27596.936$. The sheath edge X_{SE} where $V_{ix}(X_{SE})=V_S=\sqrt{1+\Theta}=1.73205$ is located at $X_{SE}=27625.34$ and is marked by a vertical line. The sheath edge potential is $\Psi_{SE}=-2.04992$. The floating potential is found at $X_f=27642.996$, and the value of the floating potential is $\Psi_f=-4.66585$. The sheath thickness is therefore $X_f-X_{SE}=17.656$, and the sheath potential drop is $\Psi_{SE}-\Psi_f=2.61593$. Both methods therefore give similar values of the sheath thickness and potential drop. With the critical ion velocity method, it is possible to determine also the position X_{MSE} of the magnetized pre-sheath edge and the respective potential Ψ_{MSE} . The obtained values are $X_{MSE}=26916.415$ and $\Psi_{MSE}=-1.03828$, but they are not shown in the figure. So, the thickness of the Chodura layer is $X_{SE}-X_{MSE}=708.925$, and the respective potential drop is $\Psi_{MSE}-\Psi_{SE}=1.01164$. From $K=500$ and $\varepsilon=10^{-5}$, it is easy to find using (22)–(24) that one $r_{Li}=200 \lambda_D$. So, the thickness of the Chodura layer is approximately $3.5 r_{Li}$.

In Fig. 13, dependence of the sheath thickness X_f-X_{SE} and the sheath potential drop $\Psi_{SE}-\Psi_f$ on ion temperature Θ , found by the KGG method, is presented. The following parameters are selected: $K=200$, $\alpha=20^\circ$, $Z=2$, $\mu=1/3670.48$, and $\varepsilon=10^{-5}$. The ion temperature Θ is gradually increased, and every time, the system of Eqs. (27)–(31) is solved using the boundary conditions (41) with $V_0=\sqrt{1+\Theta}$. The ion temperature is varied over 4 orders of magnitude, from $\Theta=10^{-4}$, to $\Theta=2$. All four source terms are used. The plots are in semi-log scale. Over a wide range of ion temperatures—up to approximately $\Theta=0.03$ —the sheath thickness X_f-X_{SE} (plot (a)) and the sheath potential drop $\Psi_{SE}-\Psi_f$ (graph (d)) remain almost constant. For larger ion temperatures, the sheath potential drop and the sheath thickness both decrease as Θ increases. In plot (a), the curves that correspond to the zero (12) and the cosine (15) source term cannot be distinguished. On the expanded scale—plot (b)—it can be seen that sheath thickness X_f-X_{SE} found with the zero source term (12) is slightly larger. Similar is valid also for the curves that correspond to the constant (13) and the exponential (14) source term. In plot (a), these lines cannot be distinguished, but expanded scale—graph (c)—reveals that sheath thickness obtained with the exponential source term (14) is slightly larger. In graph (d), the sheath potential drop $\Psi_{SE}-\Psi_f$ is plotted versus Θ for all four source terms (12)–(15). In this graph, the differences between different source terms cannot be seen. In plot (e), a small part of graph (d) is shown on an expanded scale. There, it can be seen that the sheath potential drop is the smallest for the constant source term (13) but the difference between the cosine (15) and the zero (12) source term is so small even for this scale.

In Figs. 14–16, very similar results are shown; only this time, the critical ion velocity method is used. In Figs. 14 and 15, the non-zero source terms (13)–(15) are analyzed, while the zero source term (12) is examined in Fig. 16. With the critical ion velocity method, one finds the positions of the magnetized pre-sheath edge X_{MSE} , using the Bohm-Chodura criterion $V_{par}=V_S$. The sheath edge position X_{SE} is found

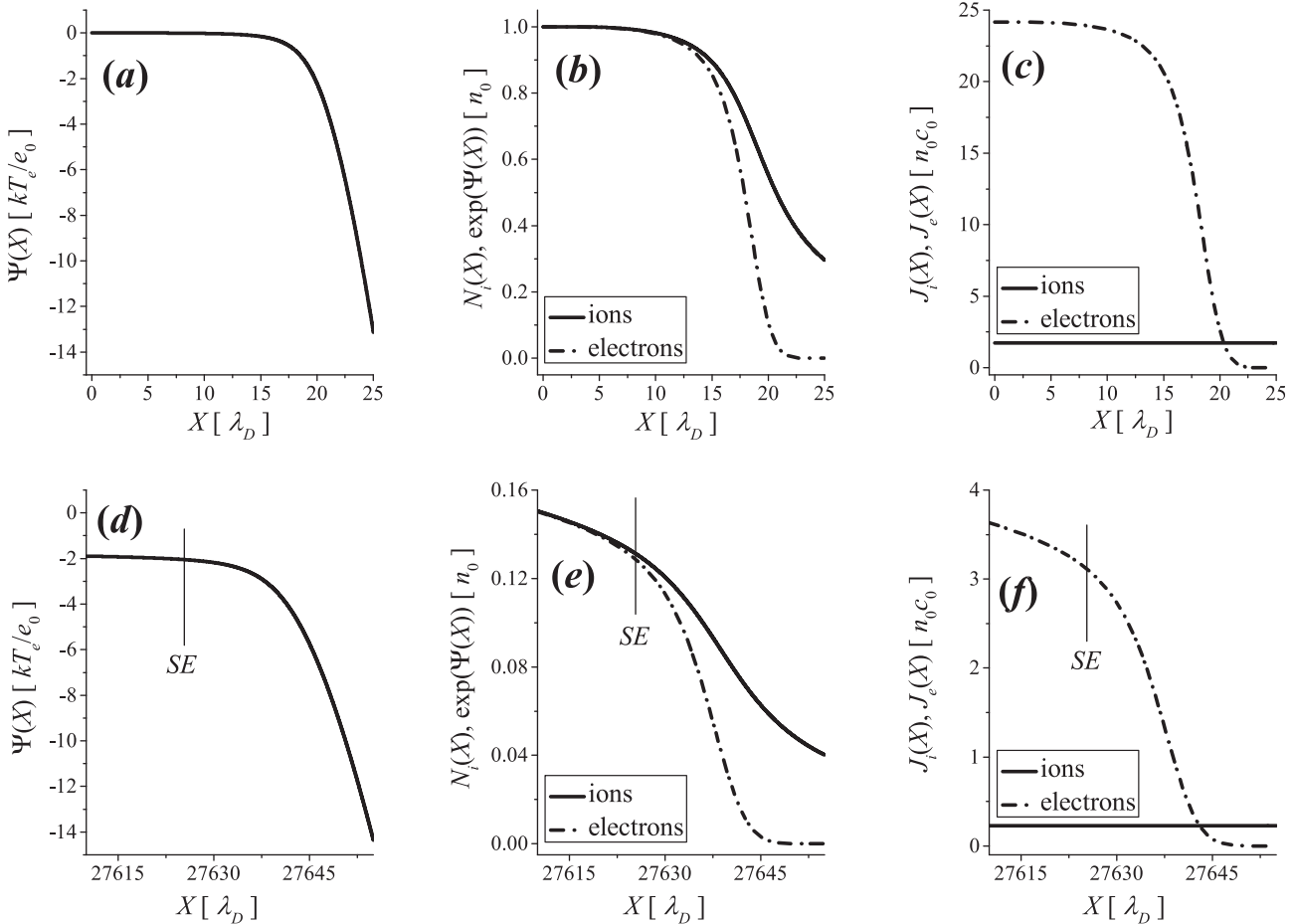


FIG. 12. Solutions of the system (27)–(31) using the boundary conditions (41), with $V_0 = V_S = \sqrt{1 + \Theta}$ and parameters: $K = 500$, $\alpha = 20^\circ$, $Z = 2$, $\Theta = 2$, $\mu = 1/3670.48$, and $\varepsilon = 10^{-5}$ are shown in the top graphs (a)–(c). In the bottom plots (d)–(f), the solutions of the same system of equations with the same parameters are displayed; only this time, the critical ion velocity method is used. The position of the sheath edge (SE) is marked by a vertical line.

using the Bohm criterion $V_{ix} = V_S$. The position of the floating electrode X_f is found using (47). All of them are measured with respect to the same origin $X = 0$ in the “center” of the discharge. The respective potentials Ψ_{MSE} , Ψ_{SE} , and Ψ_f are also measured with respect to the zero potential at $X = 0$.

In the top graphs (a), (b), and (c) in Fig. 14, the positions X_{MSE} , X_{SE} , and X_f are plotted versus Θ . The respective potentials Ψ_{MSE} , Ψ_{SE} , and Ψ_f are shown in the bottom graphs (d), (e), and (f). The following parameters are selected: $K = 200$, $\alpha = 20^\circ$, $Z = 2$, $\mu = 1/3670.48$, and $\varepsilon = 10^{-5}$. The non-zero source terms (13)–(15) are used. Curves that correspond to different source terms are marked by a legend in the graphs. Boundary conditions are given by (40) with $V_0 = 10^{-8}$ for all three source terms. From plots (d) and (e), one sees that the potentials Ψ_{MSE} and Ψ_{SE} do not depend on Θ . The floating potential Ψ_f is almost constant over a wide range of ion temperatures, but when Θ exceeds approximately 0.1, Ψ_f starts to increase with the increase in Θ . Similar is valid also for the values of X_{MSE} , X_{SE} , and X_f , displayed in plots (a), (b), and (c). Since $\varepsilon = 10^{-5}$, the values of X_{MSE} , X_{SE} and X_f , measured in units of λ_D , are rather large. Because the sheath is very thin in comparison with the pre-sheath length, the curves shown in plots (b) and (c), corresponding to the same source term, could not be distinguished if they were presented in the same graph. In order to obtain the dependence

of the sheath thickness $X_f - X_{SE}$, of the Chodura layer thickness $X_{SE} - X_{MSE}$, and of the respective potential drops $\Psi_{SE} - \Psi_f$ and $\Psi_{MSE} - \Psi_{SE}$ on Θ , one has to subtract the curves shown in Fig. 14 appropriately from one another. The results are shown in Fig. 15. The sheath potential drop $\Psi_{SE} - \Psi_f$ versus Θ is shown in plot (a) and the sheath thickness $X_f - X_{SE}$ in plot (b). The dependence of the magnetic pre-sheath potential drop $\Psi_{MSE} - \Psi_{SE}$ on Θ is presented in graph (c). The thickness of the Chodura layer $X_{SE} - X_{MSE}$ is shown in plot (d). The potential drop $\Psi_{MSE} - \Psi_{SE}$ in the Chodura layer does not depend on Θ . The thickness of the Chodura layer $X_{SE} - X_{MSE}$ is almost independent of Θ in a wide range of ion temperatures from $\Theta = 10^{-4}$ to approximately $\Theta \sim 0.1$. For larger Θ , the thickness $X_{SE} - X_{MSE}$ starts to increase with the increase in Θ . At low Θ , the thickness $X_{SE} - X_{MSE}$ is between $440 \lambda_D$ for the constant source term (13) and $580 \lambda_D$ for the exponential source term (14). At the largest ion temperature considered, which is $\Theta = 2$, the thickness $X_{SE} - X_{MSE}$ is between $760 \lambda_D$ for the constant source term (13) and $1000 \lambda_D$ for the exponential source term (14). From $K = 200$ and $\varepsilon = 10^{-5}$, it is easy to calculate that one ion Larmor radius r_{Li} corresponds to 500 Debye lengths λ_D . So, the thickness $X_{SE} - X_{MSE}$ of the Chodura layer varies approximately between 1 and 2 ion Larmor radii. In plot (b), the sheath thickness $X_f - X_{SE}$ is displayed versus

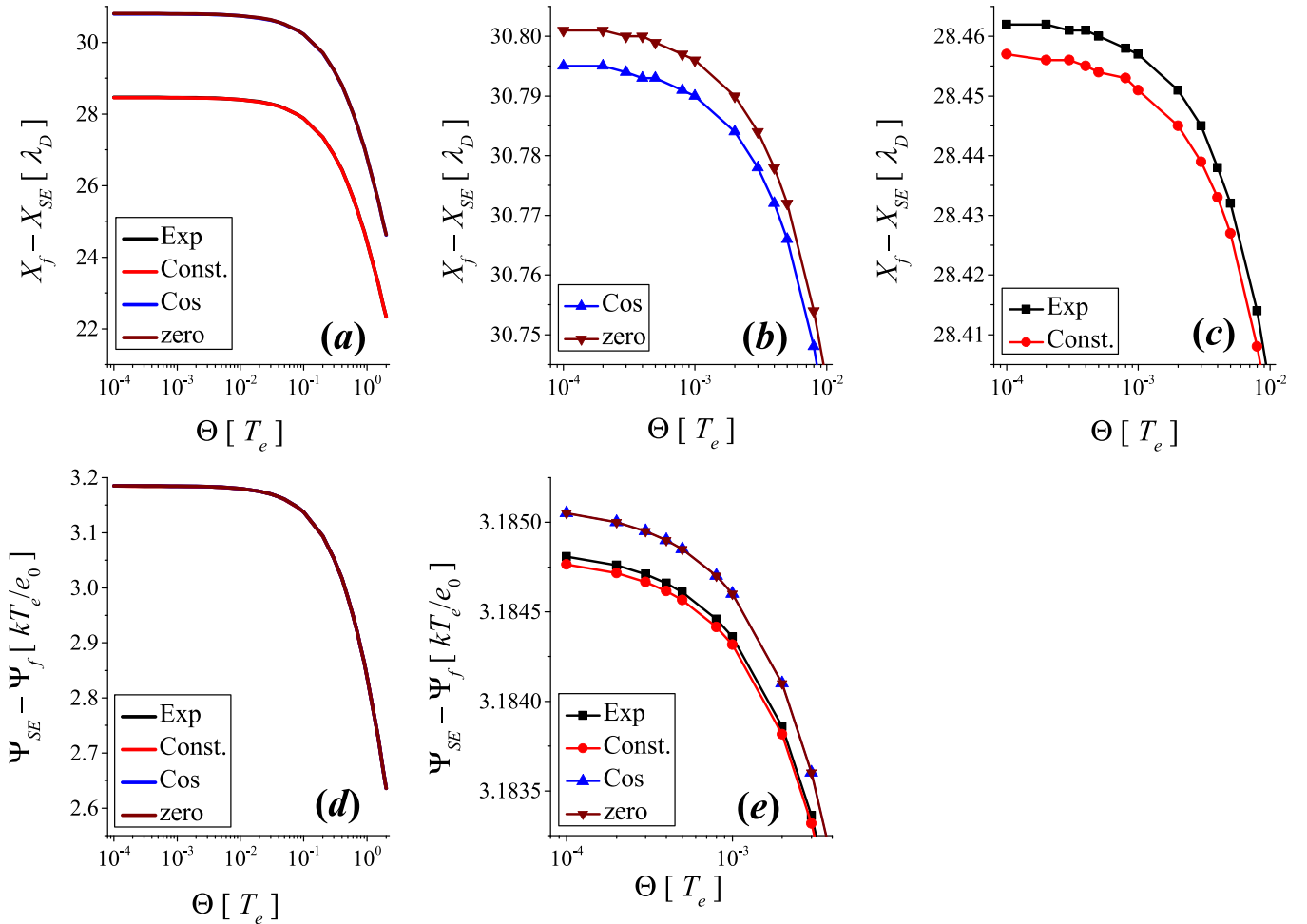


FIG. 13. The sheath thickness $X_f - X_{SE}$ (top plots (a)–(c)) and the sheath potential drop $\Psi_{SE} - \Psi_f$ (bottom graphs (d) and (e)) versus the ion temperature Θ obtained by the KGG method. The parameters are: $K = 200$, $\alpha = 20^\circ$, $Z = 2$, $\mu = 1/3670.48$, and $\varepsilon = 10^{-5}$. In graphs (b) and (c), parts of plot (a) are shown on an expanded scale. In plot (e), a part of figure (d) is presented on an expanded scale. Legends in the graphs indicate which lines and symbols correspond to different source terms.

Θ . In a wide range of ion temperatures between $\Theta = 10^{-4}$ and approximately $\Theta \sim 0.1$, it is almost independent of Θ . For larger Θ , it starts to decrease with the increase in Θ . The order of magnitude of the sheath thickness is around $30 \lambda_D$, which is roughly 20 times smaller than the thickness of the Chodura layer. The choice of different source terms (13), (14), and (15) leads to relatively small differences between the results shown in Figs. 14 and 15—graphs (b), (c), and (d). A kind of exception from this rule is the sheath potential drop $\Psi_{SE} - \Psi_f$, which is plotted versus Θ in Fig. 15(a). Here, the curves that correspond to different source terms (13)–(15) are so close to one another that they cannot be distinguished on the graph that is presented in full scale. Very small differences can only be noticed on a strongly expanded scale, shown in the inset of Fig. 15(a).

In Fig. 16, similar analysis, as shown in Figs. 14 and 15 for the non-zero source terms (13)–(15), is presented for the zero source term (12). The same parameters as in the previous two figures are selected: $K = 200$, $\alpha = 20^\circ$, $Z = 2$, $\mu = 1/3670.48$, and $\varepsilon = 10^{-5}$. Boundary conditions are given by (40), but this time, two different velocities V_0 are selected, $V_0 = 0.020$ and $V_0 = 0.022$. The curves that correspond to each of these velocities are marked in the legend in

the graphs. In plot (a), the positions X_{MSE} , X_{SE} , and X_f are plotted versus Θ , while the respective potentials Ψ_{MSE} , Ψ_{SE} , and Ψ_f are shown in graph (d). The solid lines that show X_{MSE} , X_{SE} , and X_f versus Θ for $V_0 = 0.020$ are so close together that they can not be distinguished. The same is valid also for the dotted lines, which represent X_{MSE} , X_{SE} , and X_f versus Θ for $V_0 = 0.022$. The values of X_{MSE} , X_{SE} , and X_f are roughly 20 times larger than the corresponding values for the non-zero source terms (13)–(15) shown in Figs. 14(a)–14(c). Dependence of X_{MSE} , X_{SE} , and X_f on Θ is qualitatively similar in both cases. With the increase in Θ , X_{MSE} , X_{SE} , and X_f increase also; only for the zero source term, the increase is slightly faster. Comparison of the potentials Ψ_{MSE} , Ψ_{SE} , and Ψ_f shown in Figs. 14(d)–14(f) on one hand and in Fig. 16(d) on the other gives somewhat different picture. For the non-zero source terms (Figs. 14(d) and 14(e)), the magnetized pre-sheath edge potential Ψ_{MSE} and the sheath edge potential Ψ_{SE} are independent of Θ , while for the zero source term (Fig. 16(d)), they both decrease with the increase in Θ . The floating potential Ψ_f on the other hand increases with the increase in Θ when the non-zero source terms are used (Fig. 14(f)), but it is independent of Θ , when the zero source term is used (Fig. 16(d)). If the zero source term is used, the

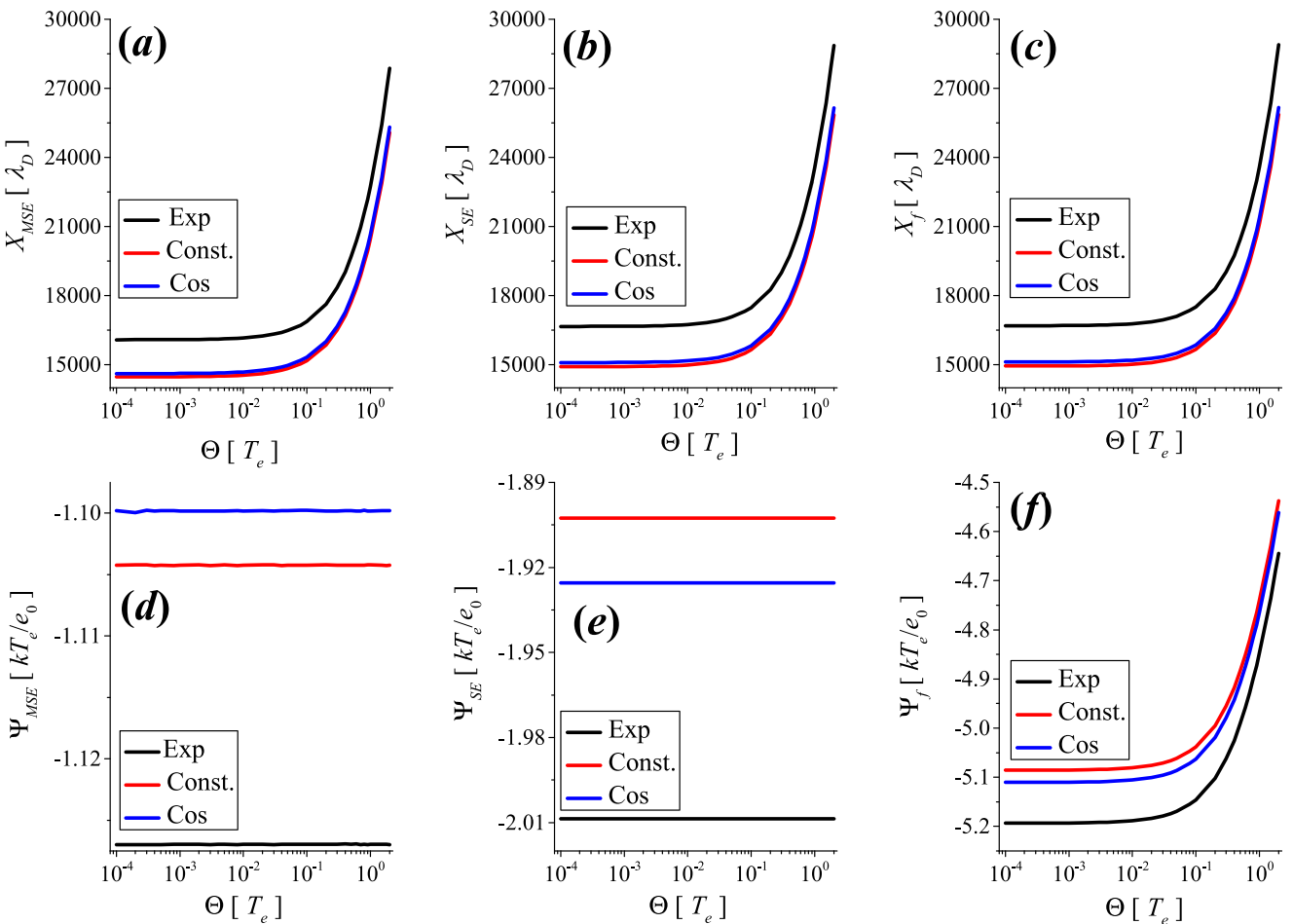


FIG. 14. Top plots: (a)— X_{MSE} versus Θ , (b)— X_{SE} versus Θ , and (c)— X_f versus Θ . Bottom graphs: (d)— Ψ_{MSE} versus Θ , (e)— Ψ_{SE} versus Θ , and (f)— Ψ_f versus Θ . The parameters are: $K = 200$, $\alpha = 20^\circ$, $Z = 2$, $\mu = 1/3670.48$, and $\varepsilon = 10^{-5}$. Legends in the graphs indicate which line corresponds to a given source term (13), (14), or (15). The critical ion velocity method is used to solve the system (27)–(31).

variation of V_0 affects also the potentials Ψ_{MSE} , Ψ_{SE} , and Ψ_f and not only their positions X_{MSE} , X_{SE} , and X_f . In order to obtain the dependence of the sheath thickness $X_f - X_{SE}$, of the Chodura layer thickness $X_{SE} - X_{MSE}$, and of the respective potential drops $\Psi_{SE} - \Psi_f$ and $\Psi_{MSE} - \Psi_{SE}$ on Θ , one has to subtract the curves shown in Fig. 16 appropriately from one another. In graph (b), the thickness of the Chodura layer $X_{SE} - X_{MSE}$ is plotted versus Θ . It is the same for both velocities V_0 . Dependence of Θ is qualitatively similar as for the non-zero source terms (Fig. 15(d)), this means that it increases when Θ is increased. For the zero source term $X_{SE} - X_{MSE}$ is more than 2 times larger than for the non-zero source terms. In Fig. 16(e), the sheath potential drop $\Psi_{SE} - \Psi_f$ and the magnetized pre-sheath potential drop $\Psi_{MSE} - \Psi_{SE}$ are plotted versus Θ . Both potential drops are equal for both velocities V_0 . The magnetized pre-sheath potential drop $\Psi_{MSE} - \Psi_{SE}$ does not depend on Θ , while the sheath potential drop $\Psi_{SE} - \Psi_f$ decreases as Θ increases. Such dependence on Θ is similar to the results displayed in Figs. 15(a) and 15(c). In Fig. 16(c), the dependence the sheath thickness $X_f - X_{SE}$ on Θ is displayed. Larger velocity V_0 results in smaller sheath thickness. With the increase in Θ , sheath thickness $X_f - X_{SE}$ decreases. Similar dependence of $X_f - X_{SE}$ on Θ is observed also in Figs. 13 and 15.

IV. COMPARISON WITH A TWO-FLUID MODEL

As mentioned already in the Introduction, a fluid model of the sheath in an oblique magnetic field that is based on the continuity equation (1) and momentum transport equation (2) for the ions, while for the electrons the Boltzmann relation (3) is assumed, is widely used^{2,3,16–30,32–34,36,37,44–46} and can be considered as the present state of the art in spite of the fact that some authors^{11–13} raised questions about the validity of the Boltzmann relation for the electrons in a magnetized plasma.

In a more rigorous treatment, one should not simply assume the Boltzmann relation for the electrons, but should treat them in similar way as the ions. In the simplest approach, a so-called two-fluid model could be used, where the ions and electrons are treated by continuity equation and momentum exchange equation written down for both particle species

$$\frac{\partial n_i}{\partial t} + \nabla \cdot (n_i \mathbf{u}_i) = S_i, \quad (48)$$

$$\frac{\partial n_e}{\partial t} + \nabla \cdot (n_e \mathbf{u}_e) = S_e, \quad (49)$$

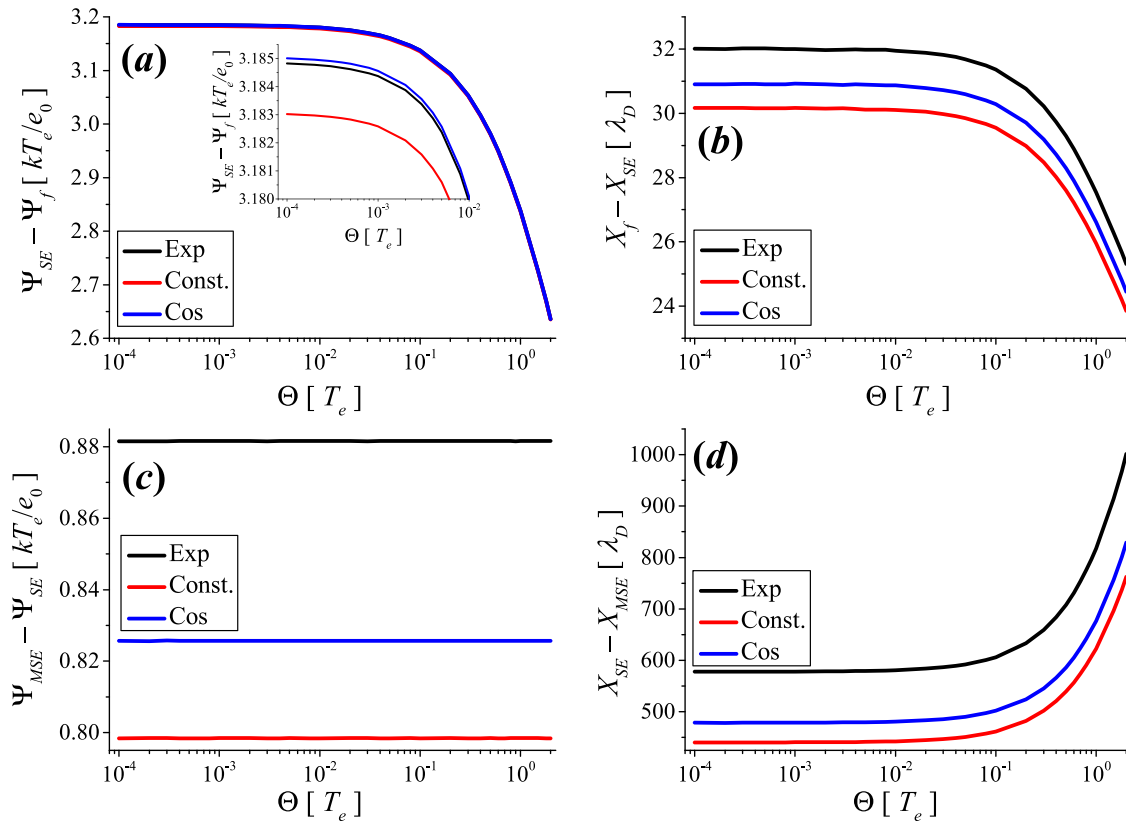


FIG. 15. In plot (a), the sheath potential drop $\Psi_{SE} - \Psi_f$ is plotted versus Θ . In the inset, a small part of the plot is shown on an expanded scale. In graph (b), the sheath thickness $X_f - X_{SE}$ is displayed versus Θ . The dependence of the magnetic pre-sheath potential drop $\Psi_{MSE} - \Psi_{SE}$ on Θ is presented in graph (c). The thickness of the Chodura layer $X_{SE} - X_{MSE}$ is shown in plot (d). The parameters are: $K = 200$, $\alpha = 20^\circ$, $Z = 2$, $\mu = 1/3670.48$, and $\varepsilon = 10^{-5}$. Legends in the graphs indicate which line corresponds to a given source term (13), (14), or (15).

$$m_i n_i \left(\frac{\partial \mathbf{u}_i}{\partial t} + (\mathbf{u}_i \cdot \nabla) \mathbf{u}_i \right) = n_i e_0 (\mathbf{E} + \mathbf{u}_i \times \mathbf{B}) - \nabla p_i + \mathbf{A}_i - m_i \mathbf{u}_i S_i, \quad (50)$$

$$m_e n_e \left(\frac{\partial \mathbf{u}_e}{\partial t} + (\mathbf{u}_e \cdot \nabla) \mathbf{u}_e \right) = -n_e e_0 (\mathbf{E} + \mathbf{u}_e \times \mathbf{B}) - \nabla p_e + \mathbf{A}_e - m_e \mathbf{u}_e S_e. \quad (51)$$

Here, \mathbf{u}_e is the electron flow velocity with the components $\mathbf{u}_e = (u_{ex}, u_{ey}, u_{ez})$, and n_e is the electron density. For the source terms S_i and S_e and also for the collisional momentum transfer terms \mathbf{A}_i and \mathbf{A}_e , some assumptions must be made. The source terms S_i and S_e can be assumed to be of one of the forms given by the formulas (12), (13), (14), or (15). For the collisional momentum transfer terms \mathbf{A}_i and \mathbf{A}_e , the following form is usually assumed:⁴⁸

$$\mathbf{A}_i = -m_i n_i \nu_{ie} (\mathbf{u}_i - \mathbf{u}_e), \quad (52)$$

$$\mathbf{A}_e = -m_e n_e \nu_{ei} (\mathbf{u}_e - \mathbf{u}_i). \quad (53)$$

Here, ν_{ie} and ν_{ei} are ion-electron and electron-ion collision frequencies for momentum exchange collisions. In such a model, the ions transfer their momentum only to the electrons and the electrons transfer their momentum only to the ions. For more details, see, e.g., Ref. 53. The conservation of the total momentum of the ions and electrons requires

$$m_i n_i \nu_{ie} = m_e n_e \nu_{ei}. \quad (54)$$

The electrons are assumed to be isothermal with a constant temperature T_e . Using similar arguments, as have been presented in formulas (5)–(9), the gradient pressure terms ∇p_i and ∇p_e are written in the following way:

$$\nabla p_i = k T_i \nabla n_i, \quad \nabla p_e = k T_e \nabla n_e. \quad (55)$$

By taking into account (52)–(55), the equations (50) and (51) are written in the following way:

$$m_i n_i \left(\frac{\partial \mathbf{u}_i}{\partial t} + (\mathbf{u}_i \cdot \nabla) \mathbf{u}_i \right) = n_i e_0 (\mathbf{E} + \mathbf{u}_i \times \mathbf{B}) - k T_i \nabla n_i - m_e n_e \nu_{ei} (\mathbf{u}_i - \mathbf{u}_e) - m_i \mathbf{u}_i S_i, \quad (56)$$

$$m_e n_e \left(\frac{\partial \mathbf{u}_e}{\partial t} + (\mathbf{u}_e \cdot \nabla) \mathbf{u}_e \right) = -n_e e_0 (\mathbf{E} + \mathbf{u}_e \times \mathbf{B}) - k T_e \nabla n_e - m_e n_e \nu_{ei} (\mathbf{u}_e - \mathbf{u}_i) - m_e \mathbf{u}_e S_e. \quad (57)$$

The model is one dimensional, so the equations (10) and (11) are valid. The steady state is analyzed, so time derivatives are set to zero. The coordinate system shown in Fig. 2 is used. The variables (22)–(24) are introduced, and the equations (48), (49), (56), (57) together with the Poisson Eq. (4) are written in the following form:

$$\frac{d}{dX} (N_i V_{ix}) = s_i, \quad (58)$$

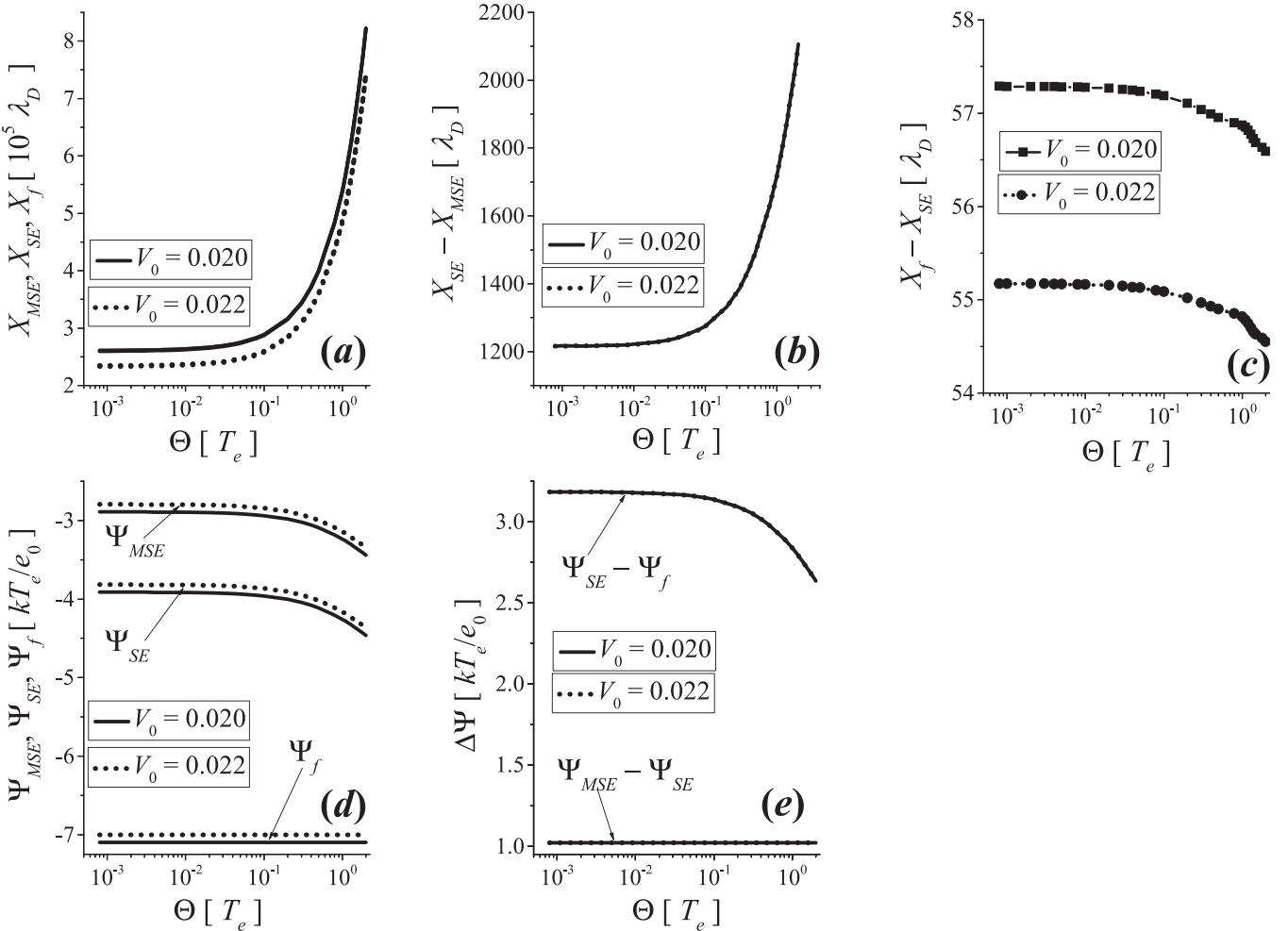


FIG. 16. In plot (a), positions X_{MSE} , X_{SE} , and X_f are plotted versus the ion temperature Θ . In figure (d), the respective potentials Ψ_{MSE} , Ψ_{SE} , and Ψ_f are displayed. The parameters are: $K = 200$, $\alpha = 20^\circ$, $Z = 2$, $\mu = 1/3670.48$, and $\varepsilon = 10^{-5}$, and the zero source term (12) is used. Two different velocities V_0 are used as boundary condition in (41). The curves that correspond to $V_0 = 0.020$ and to $V_0 = 0.022$ are marked by legend in each graph.

$$\frac{d}{dX}(N_e V_{ex}) = s_e, \quad (59)$$

$$N_i V_{ix} \frac{dV_{ix}}{dX} = -N_i \frac{d\Psi}{dX} - \Theta \frac{dN_i}{dX} - K \cos(\alpha) N_i V_{iz} - \mu N_e Z_{ei} (V_{ix} - V_{ex}) - V_{ix} s_i, \quad (60)$$

$$N_e V_{ex} \frac{dV_{ex}}{dX} = \frac{1}{\mu} N_e \frac{d\Psi}{dX} - \frac{1}{\mu} \frac{dN_e}{dX} + \frac{K}{\mu} \cos(\alpha) N_e V_{ez} - N_e Z_{ei} (V_{ex} - V_{ix}) - V_{ex} s_e, \quad (61)$$

$$N_i V_{ix} \frac{dV_{iy}}{dX} = K \sin(\alpha) N_i V_{iz} - \mu N_e Z_{ei} (V_{iy} - V_{ey}) - V_{iy} s_i. \quad (62)$$

$$N_e V_{ex} \frac{dV_{ey}}{dX} = -\frac{K}{\mu} \sin(\alpha) N_e V_{ez} - N_e Z_{ei} (V_{ey} - V_{iy}) - V_{ey} s_e. \quad (63)$$

$$N_i V_{ix} \frac{dV_{iz}}{dX} = K \cos(\alpha) N_i V_{ix} - K \sin(\alpha) N_i V_{iy} - \mu N_e Z_{ei} (V_{iz} - V_{ez}) - V_{iz} s_i. \quad (64)$$

$$N_e V_{ex} \frac{dV_{ez}}{dX} = -\frac{K}{\mu} \cos(\alpha) N_e V_{ex} + \frac{K}{\mu} \sin(\alpha) N_e V_{ey} - N_e Z_{ei} (V_{ez} - V_{iz}) - V_{ez} s_e, \quad (65)$$

$$\varepsilon^2 \frac{d^2 \Psi}{dX^2} = -(N_i(X) - N_e(X)). \quad (66)$$

The space coordinate has been normalized to the ionization length, $X = \frac{x}{L}$, while the coefficients s_i and s_e that correspond to different source terms (12), (13), (14) or (15), are given in Table III. In addition, the following variables have been introduced:

$$N_e = \frac{n_e}{n_0}, \quad V_{ex} = \frac{u_{ex}}{c_0}, \quad V_{ey} = \frac{u_{ey}}{c_0}, \\ V_{ez} = \frac{u_{ez}}{c_0}, \text{ and } Z_{ei} = \nu_{ei} \tau. \quad (67)$$

The system of equations (58)–(66) is solved numerically in similar way as the system (27)–(31). The integration starts at $X = 0$ and proceeds in the positive x direction towards the electrode. The boundary values at $X = 0$ are given by

$$N_i(0) = N_e(0) = 1, \quad \Psi(0) = \frac{d\Psi}{dX}(0) = 0, \\ V_{iy}(0) = V_{iz}(0) = V_{ey}(0) = V_{ez}(0) = 0, \\ V_{ix}(0) = V_{ex}(0) = V_0. \quad (68)$$

But before any attempt of numerical solution is made, let us take a look at the Eq. (61) and let us assume that there

TABLE III. The coefficients s_i and s_e that correspond to four different source terms (12), (13), (14), or (15) in the systems of Eqs. (58)–(66).

Coefficient	Zero source term (12)	Constant source term (13)	Exponential source term (14)	Cosine source term (15)
s_i	0	1	$N_e(X)$	$\cos\left(\frac{\pi V_{ix}}{2 V_S}\right) H(V_S - V_{ix})$
s_e	0	1	$N_e(X)$	$\cos\left(\frac{\pi V_{ix}}{2 V_S}\right) H(V_S - V_{ix})$

is no magnetic field, no collisions, and no ionizations, $K=Z_{ei}=s_e=0$. Let us also assume that the dependence of the electron velocity V_{ex} on X is so weak that also the derivative on the left hand side can be neglected. Eq. (61) is then transformed into:

$$N_e \frac{d\Psi}{dX} - \frac{dN_e}{dX} = 0, \quad (69)$$

with the solution

$$N_e = \exp(\Psi) + \text{Const.} \quad (70)$$

This is the Boltzmann relation. So, if the Boltzmann relation is assumed for the electrons, this implies that (1) there is no creation or annihilation of electrons, or in other words, $s_e=0$ and (2) the electrons do not suffer any momentum exchange collisions, or $Z_{ei}=0$. If only one species of positive ions and electrons is present in the plasma, then also the ion source term S_i should be zero, since it is not possible to imagine an ionization mechanism, where only ions, but no electrons, would be created and annihilated.

Let us now illustrate this further by comparison of the numerical solutions of the system (27)–(31) on one hand and of the system (58)–(66) on the other. If a direct comparison is to be made, obviously, momentum exchange collisions must be excluded $Z=Z_{ei}=0$. In Fig. 17, an example of the solutions of both systems is shown. The system (58)–(66) is

solved for the following parameters: $K=100$, $\alpha=20^\circ$, $\Theta=0$, $Z_{ei}=0$, $\varepsilon=10^{-5}$, $\mu=1/400$, and $\mu=1/900$. The constant source term (13) is selected, and the space coordinate is normalized to L . The boundary conditions (68) with $V_0=10^{-7}$ are used. The system (58)–(66) is solved 4 times. The first time $s_i=s_e=1$ is assumed and $\mu=1/400$ is selected. The second solution is obtained using $s_i=s_e=1$ and $\mu=1/900$. For the third solution $s_i=1$, $s_e=0$, and $\mu=1/400$ are taken. The fourth solution is obtained using $s_i=1$, $s_e=0$, and $\mu=1/900$. By taking $\mu=1/400$ and $\mu=1/900$, the electron mass is increased artificially in order to illustrate better its effect to the solution. The selection of different source terms for ions and electrons, $s_i=1$, $s_e=0$, breaks the consistency of the model, but it is done deliberately in order to illustrate the effect. In graphs (a) and (c), the potential profiles $\Psi(X)$ and ion density profiles $N_i(X)$ for all four solutions are shown in full scale. In this scale, the curves that correspond to different solutions cannot be distinguished. In graphs (b) and (d), small parts of plots (a) and (c) are shown on a strongly expanded scale. The first solution ($s_i=s_e=1$, $\mu=1/400$) is shown by both lines A. Curves B in plots (b) and (d) correspond to the second solution ($s_i=s_e=1$, $\mu=1/900$). The third ($s_i=1$, $s_e=0$, $\mu=1/400$) and the fourth ($s_i=1$, $s_e=0$, $\mu=1/900$) solution are shown by curves C. The third and the fourth solution are so close together that they cannot be distinguished even on an expanded scale. As the electron to ion mass ratio μ is decreased, the

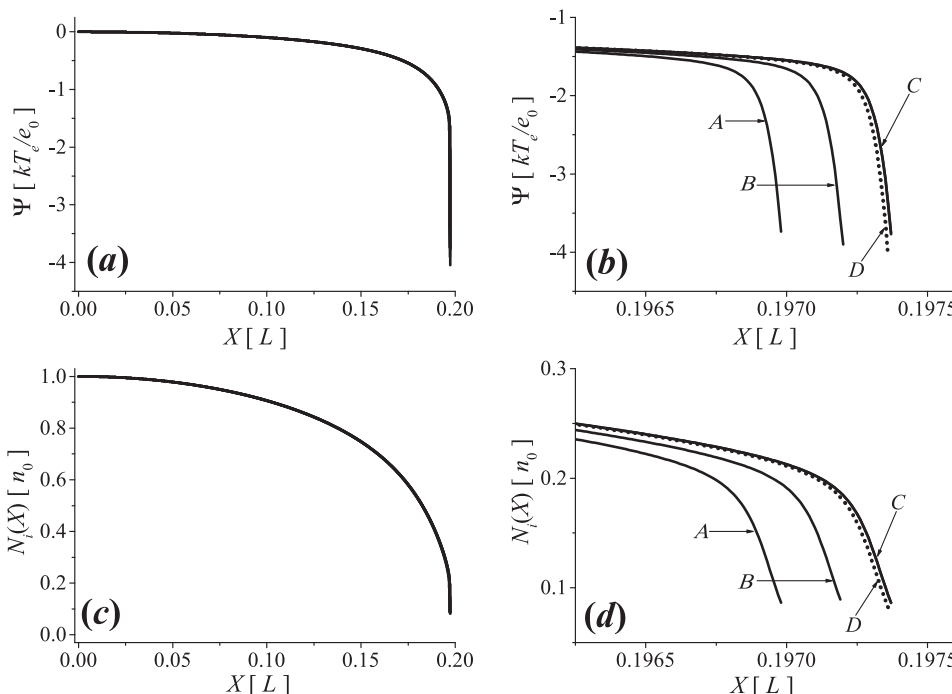


FIG. 17. Solutions of the systems (27)–(31) and (58)–(66) for the parameters $K=100$, $\alpha=20^\circ$, $\Theta=0$, $Z=Z_{ei}=0$, $\varepsilon=10^{-5}$, $\mu=1/400$, and $\mu=1/900$. In graphs (a) and (b), potential profiles $\Psi(X)$ are shown, while in plots (c) and (d), the ion density profiles $N_i(X)$ are presented. In plots (b) and (d), small parts of graphs (a) and (c) are shown on an expanded scale. Labels of the curves A, B, C, and D in graphs (b) and (d) are explained in the text.

solutions obtained with the consistent selection of source terms ($s_i = s_e$) come closer and closer to the solution obtained with the inconsistent selection of source terms ($s_i \neq 0$ and $s_e = 0$).

The system (27)–(31) is solved for the parameters $K = 100$, $\alpha = 20^\circ$, $\Theta = 0$, $Z = 0$, $\varepsilon = 10^{-5}$ using the boundary conditions (41) with $V_0 = 10^{-7}$. Also in this case, the normalization of the space coordinate $X = \frac{x}{L}$ is selected. With $Z = 0$ and the constant source term (13), one finds in Table II that $S_1 = S_2 = 1$. The potential $\Psi(X)$ and ion density $N_i(X)$ profiles that are found are also shown in Fig. 17. In graphs (a) and (c), the curves that correspond to the solution of the system (27)–(31) cannot be distinguished from the curves that represent the above mentioned solutions of the system (58)–(66). Only on the expanded scale—plots (b) and (d)—the solutions of both systems of equations can be distinguished. The solutions of the system (27)–(31) are shown by dotted line—curve D. It can be noticed that curves C and D are very close together. This is because the assumption that the Boltzmann relation is valid for the electrons implies $S_e = 0$. In the absence of magnetic field, the curves C and D would overlap completely.

This example illustrates very well that assuming the Boltzmann relation for the electron density is equivalent to the assumption of the zero source term $S_e = 0$ for the electrons. If in addition to electrons only one positive ion species is present in the plasma, the only way to keep the model consistent is to put also $S_i = 0$. But, in spite of this, many authors^{3,8,9,18,22,23,32,33,35,42,44} use the model, where Boltzmann relation is assumed for electrons, while continuity and momentum exchange equations with $S_i \neq 0$ are used for the ions. Such a model is inconsistent and therefore should not be used anymore in the future.

Perhaps, the following remark can be given about the already published work that has been quite extensive and where the above mentioned inconsistent model has been used. It has been shown relatively recently that validity of the Boltzmann relation in magnetized plasmas is limited,^{11–13} but may be used in some cases. The results shown in Fig. 17 indicate that the difference between the results obtained by the inconsistent model described above, and the results found by a self-consistent two fluid model is rather small. Of course, Fig. 17 shows only one example for only one set of selected parameters. It should be verified by systematic comparison of the inconsistent model with more advanced self-consistent models (two-fluid model is a good candidate) that how big are the errors introduced by the model, which uses the Boltzmann relation for electrons and $S_i \neq 0$ for the ions. The attention should be focused to the parameters, where the conditions described in Refs. 11–13 are on one side fulfilled and on the other side strongly violated. Perhaps, in this way, the conditions could be found, where the results obtained with the inconsistent model still have some value.

V. CONCLUSIONS

A one-dimensional fluid model of the magnetized plasma-wall transition region in front of a planar floating

electrode immersed in an oblique magnetic field has been analyzed extensively. Assuming that the continuity equation and the momentum transport equation are valid for the positive ions and the Boltzmann distribution is assumed for the electrons, a system of differential equations has been derived and solved numerically. The model can be solved either in the quasi-neutral pre-sheath region only—Eqs. (33)–(36) or in the entire plasma-wall transition region—Eqs. (27)–(31). There are 4 natural length scales that can be used for the normalization of the space coordinate. These are: (1) the Debye length λ_D , (2) the ionization length L , (3) the mean free path for elastic collisions of ions L_c , and (4) the ion Larmor radius r_{Li} . The properties of the solutions do not depend on the selection of the length scale for the normalization of the space coordinate.

In the literature, mainly two forms of the ion source term S_i on the right hand side of the ion continuity Eq. (1) are assumed. These are the zero source term (12), e.g., Refs. 2, 16, 17, 19–21, 24–30, 34, 36, 45, and 46 and the exponential source term (14), e.g., Refs. 3, 8, 9, 18, 22, 23, 32, 33, 35, 37, 42, and 44. By selecting the zero source term, (12), one assumes that there is no creation or annihilation of the ions anywhere in the system. The exponential source term (14) implies that the main ionization mechanism are ionizing electron-neutral collisions, and the ionization rate is therefore proportional to the local electron density. In this work, two additional source terms have been considered. The constant source term (13) assumes a spatially uniform creation of ion-electron pairs everywhere in the system. The fourth—the cosine—source term (15) is somewhat more artificially constructed. It implies an assumption that the ionization decreases, as the ion velocity V_{ix} increases, as the ions are accelerated in the pre-sheath towards the collector and then drops to zero when V_{ix} reaches the ion sound velocity V_s . In this way, there is spatially dependent ionization in the pre-sheath, but there is no ionization in the sheath.

A comparison with a two-fluid model has been made, and it has been shown that the assumption of Boltzmann distributed electrons implies that there is no creation or annihilation of the electrons in the system. If only one positive ion species and electrons are present in the system, the model is consistent only if the zero source term $S_i = 0$ is selected for the ions. The model which uses the Boltzmann relation for the electrons and $S_i \neq 0$ at the same time is therefore inconsistent and should not be used anymore in the future. Nevertheless, such inconsistent model has been widely used^{3,8,9,18,22,23,32,33,35,37,42,44} in the past and even relatively recently. In this work, an extensive comparison of the results obtained by the consistent ($S_i = 0$) and by the inconsistent ($S_i \neq 0$) model has therefore been performed.

It has been shown that there is a large difference between the solutions of the systems of Eqs. (27)–(31) and (33)–(36) when the zero source term is used on one hand and when the non-zero source terms are selected on the other hand. If the zero source term is used, the systems of Eqs. (27)–(31) and (33)–(36) become very sensitive to the boundary conditions, especially to the selection of the ion velocity V_0 at the starting point. If a very small V_0 is selected, the solutions of the systems (27)–(31) and (33)–(36) predict very

extended pre-sheath regions, and in some cases (when V_0 is below $\sim 10^{-6}$), also problems related to poor convergence of the numerical solutions can be observed. In addition, the solutions exhibit oscillations, which may have rather large amplitude, especially if the frequency of elastic collisions is low. Physical explanation of these oscillations requires a separate study, which is beyond the scope of this paper. The model with $S_i=0$ has been used extensively in the literature.^{2,16,17,19–21,24–30,34,36,45,46} It is interesting that the authors almost never talk about the above mentioned problems, although they present non-monotonic solutions in their figures.

If on the other hand any of the three remaining non-zero ion source terms is selected, problems related to the oscillatory solutions and their extreme sensitivity to V_0 are eliminated. Although three different forms of the non-zero source terms have been used, they all give almost identical results. But unfortunately, by selecting any of the non-zero source terms, also the consistency of the model is broken. Although such model is not consistent, and should therefore not be used anymore in the future, numerous results already obtained by this model should not be simply thrown away. Instead, they should be evaluated by a systematic comparison with more advanced self-consistent models, like, for example, the two-fluid model. One example of such comparison is shown in Fig. 17.

A one-dimensional fluid model of the magnetized plasma-wall transition in front of a planar floating electrode immersed in an oblique magnetic field, which is based on the use of the continuity equation and the momentum transport equation for the positive ions, while the Boltzmann relation is assumed for the electrons has also been extensively used for the analysis of the ion temperature effects.^{19–24} The ions are assumed to be isothermal, and the gradient pressure term in the momentum exchange equation is replaced by the ion density gradient multiplied by a constant ion temperature which can be varied. In Refs. 19–24 and also in some other papers, the problem is analyzed in the sheath scale only. The boundary conditions (40) with $V_0=V_S$ are applied at the sheath edge, and the system (27)–(31) is integrated, usually until the floating potential is reached. In this way, the potential, density, and velocity profiles inside the sheath are obtained, but no information can be obtained about the pre-sheath region. In this paper, such an approach is called the KGG method after.¹⁹ The KGG method also eliminates one tricky problem. This problem lies in the fact that as soon as the ion temperature is larger than zero, the system (27)–(31) becomes stiff, unless the boundary velocity of ions V_0 is increased above the critical value, which is slightly above the ion thermal velocity.

In this work, an alternative method to analyze the ion temperature effect has been proposed. It has been called the critical ion velocity method, and it is based on the fact that the pre-sheath system (33)–(36) can be solved using boundary conditions (41) with a very small value of V_0 also in the case when the ion temperature is larger than zero. The system (33)–(36) is then integrated until the ion velocity exceeds the critical value, which then makes the solution of the system (27)–(31) possible. The potential, electric field,

ion density, and ion velocity in this point are recorded and used as boundary conditions (40) for the integration of the system (27)–(31). As opposed to the KGG method, where only the Bohm criterion is fulfilled at the sheath edge, the critical ion velocity method gives also the location where the Bohm-Chodura criterion is fulfilled, if the parameters have the values, which lead to the formation of the Chodura layer. The critical ion velocity method therefore allows the position and the potential of the magnetized pre-sheath edge to be determined. Consequently, this allows to determine the thickness and the potential drop of the Chodura layer. The method has been tested for all four source terms considered in this paper. For all four source terms, the sheath thickness and the sheath potential drop decrease with an increase in ion temperature. For all four source terms, the thickness of the Chodura layer increases with an increase in ion temperature, while the potential drop in the Chodura layer does not depend on ion temperature. But, there is also an interesting difference between the results obtained with non-zero source terms on one hand and with the zero source term on the other. When the zero source term is used, the floating potential Ψ_f does not depend on ion temperature, while the sheath edge potential Ψ_{SE} and the magnetized pre-sheath edge potential Ψ_{MSE} both decrease with ion temperature increasing. When the non-zero source terms are used, the sheath edge potential Ψ_{SE} and the magnetized pre-sheath edge potential Ψ_{MSE} do not depend on ion temperature, while the floating potential Ψ_f increases with the increase in ion temperature.

ACKNOWLEDGMENTS

This work has been partially supported by Grant No. P2-0073 of the Slovenian research agency.

- ¹R. Chodura, *Phys. Fluids* **25**, 1628 (1982).
- ²K.-U. Riemann, *Phys. Plasmas* **1**, 552 (1994).
- ³K.-U. Riemann, *Contrib. Plasma Phys.* **34**, 127 (1994).
- ⁴P. C. Stangeby, *Phys. Plasmas* **2**, 702 (1995).
- ⁵I. H. Hutchinson, *Phys. Plasmas* **3**, 6 (1996).
- ⁶E. Ahedo, *Phys. Plasmas* **4**, 4419 (1997).
- ⁷I. I. Beilis and M. Keidar, *Phys. Plasmas* **5**, 1545 (1998).
- ⁸N. Sternberg and J. Poggie, *IEEE Trans. Plasma Sci.* **32**, 2217 (2004).
- ⁹R. N. Franklin, *J. Phys. D: Appl. Phys.* **38**, 3412 (2005).
- ¹⁰D. D. Tskhakaya, Sr. and L. Kos, *Phys. Plasmas* **21**, 102115 (2014).
- ¹¹J. E. Allen, *Contrib. Plasma Phys.* **48**, 400 (2008).
- ¹²R. N. Franklin, *J. Plasma Phys.* **78**, 21 (2012).
- ¹³T. M. G. Zimmermann, M. Coppins, and J. E. Allen, *Phys. Plasmas* **17**, 022301 (2010).
- ¹⁴S. F. Masoudi, *Vacuum* **81**, 871 (2007).
- ¹⁵S. F. Masoudi, S. S. Esmaeili, and S. Jazavandi, *Vacuum* **84**, 382 (2009).
- ¹⁶S. F. Masoudi and S. M. Salehkoutaki, *Eur. Phys. J. D* **57**, 71 (2010).
- ¹⁷S. F. Masoudi, *Eur. Phys. J. D* **64**, 369 (2011).
- ¹⁸T. M. G. Zimmermann, M. Coppins, and J. E. Allen, *Phys. Plasmas* **15**, 072301 (2008).
- ¹⁹M. Khoramabadi, H. Ghomi, and M. Ghorannevis, *J. Fusion Energy* **29**, 365 (2010).
- ²⁰M. Khoramabadi, H. Ghomi, and P. K. Shukla, *J. Appl. Phys.* **109**, 073307 (2011).
- ²¹M. El Koauini, H. Chatei, I. Driouch, and M. El Hammouti, *J. Fusion Energy* **30**, 199 (2011).
- ²²J. Liu, F. Wang, and J. Sun, *Phys. Plasmas* **18**, 013506 (2011).
- ²³J. Ou and J. Yang, *Phys. Plasmas* **19**, 113504 (2012).
- ²⁴M. M. Hatami and B. Shokri, *Phys. Plasmas* **19**, 083510 (2012).
- ²⁵M. M. Hatami, A. R. Niknam, and B. Shokri, *Vacuum* **83**, S231 (2009).

- ²⁶M. M. Hatami, B. Shokri, and A. R. Niknam, *J. Phys. D: Appl. Phys.* **42**, 025204 (2009).
- ²⁷M. M. Hatami, A. R. Niknam, B. Shokri, and H. Ghomi, *Phys. Plasmas* **15**, 053508 (2008).
- ²⁸M. M. Hatami, *Phys. Plasmas* **20**, 083501 (2013).
- ²⁹A. K. Shaw, S. Kar, K. S. Goswami, and B. J. Saikia, *Phys. Plasmas* **19**, 012120 (2012).
- ³⁰M. Stanojević, J. Dušović, N. Jelić, and S. Kuhn, *Phys. Plasmas* **14**, 013504 (2007).
- ³¹M. M. Hatami and B. Shokri, *Phys. Plasmas* **20**, 033506 (2013).
- ³²K. Yasserian, M. Aslaninejad, and M. Ghoranneviss, *Phys. Plasmas* **16**, 023504 (2009).
- ³³K. Yasserian and M. Aslaninejad, *Phys. Plasmas* **17**, 023501 (2010).
- ³⁴K. Yasserian and M. Aslaninejad, *Phys. Plasmas* **19**, 073507 (2012).
- ³⁵K. Yasserian and M. Aslaninejad, *Phys. Lett. A* **378**, 2757 (2014).
- ³⁶A. K. Shaw, S. Kar, K. S. Goswami, and B. J. Saikia, *Phys. Plasmas* **19**, 102108 (2012).
- ³⁷K. Yasserian and M. Aslaninejad, *Phys. Plasmas* **19**, 033504 (2012).
- ³⁸D. D. Tskhakaya, P. K. Shukla, B. Eliasson, and S. Kuhn, *Phys. Plasmas* **12**, 103503 (2005).
- ³⁹B. Alterkop, S. Goldsmith, and R. L. Boxman, *Contrib. Plasma Phys.* **45**, 485 (2005).
- ⁴⁰D. Tskhakaya and S. Kuhn, *Contrib. Plasma Phys.* **44**, 564 (2004).
- ⁴¹D. Tskhakaya and S. Kuhn, *Plasma Phys. Controlled Fusion* **47**, A327 (2005).
- ⁴²J. Kovačič, T. Gyergyek, and M. Čerček, *Eur. Phys. J. D* **54**, 383 (2009).
- ⁴³J. Loizu, P. Ricci, F. D. Halpern, and S. Jolliet, *Phys. Plasmas* **19**, 122307 (2012).
- ⁴⁴R. M. Crespo and R. N. Franklin, *Plasma Sources Sci. Technol.* **23**, 035012 (2014).
- ⁴⁵X. Zou, J.-H. Liu, Y. Gong, Z.-X. Wang, Y. Liu, and X.-G. Wang, *Vacuum* **73**, 681 (2004).
- ⁴⁶X. Zou, M. Qiu, H. Liu, L. Zhang, and Y. Gong, *Vacuum* **83**, 205 (2008).
- ⁴⁷S. Kuhn, K.-U. Riemann, N. Jelić, D. D. Tskhakaya, Sr., D. Tskhakaya, Jr., and M. Stanojević, *Phys. Plasmas* **13**, 013503 (2006).
- ⁴⁸J. A. Bittencourt, *Fundamentals of Plasma Physics* 3rd ed. (Springer-Verlag, New York, 2004).
- ⁴⁹K.-U. Riemann, *IEEE Trans. Plasma Sci.* **23**, 709 (1995).
- ⁵⁰K.-U. Riemann, *J. Tech. Phys.* **41**, 89 (2000).
- ⁵¹K.-U. Riemann, *Phys. Fluids B* **1**, 961 (1989).
- ⁵²H. Ghomi and M. Khoramabadi, *J. Plasma Phys.* **76**, 247 (2010).
- ⁵³J. P. Freidberg, *Plasma Physics and Fusion Energy* (Cambridge University Press, Cambridge, New York, Melbourne, Madrid, Cape Town, Singapore, São Paulo, 2007), Chap. IX and X.